

This work was written as part of one of the author's official duties as an Employee of the United States Government and is therefore a work of the United States Government. In accordance with 17 U.S.C. 105, no copyright protection is available for such works under U.S. Law. Access to this work was provided by the University of Maryland, Baltimore County (UMBC) ScholarWorks@UMBC digital repository on the Maryland Shared Open Access (MD-SOAR) platform.

Please provide feedback

Please support the ScholarWorks@UMBC repository by emailing scholarworks-group@umbc.edu and telling us what having access to this work means to you and why it's important to you. Thank you.

1 **Revisiting the Effectiveness of HCHO/NO₂ Ratios for**
2 **Inferring Ozone Sensitivity to Its Precursors using High**
3 **Resolution Airborne Remote Sensing Observations in a**
4 **High Ozone Episode during the KORUS-AQ Campaign**

5
6 Amir H. Souri^{1*}, Caroline R. Nowlan¹, Glenn M. Wolfe^{2,3}, Lok N. Lamsal^{2,4}, Christopher E.
7 Chan Miller¹, Gonzalo González Abad¹, Scott J. Janz², Alan Fried⁵, Donald R. Blake⁶,
8 Andrew J. Weinheimer⁷, Glenn S. Diskin⁸, Xiong Liu¹, and Kelly Chance¹

9
10 ¹Harvard-Smithsonian Center for Astrophysics, Cambridge, MA, USA

11 ²NASA Goddard Space Flight Center, Greenbelt, MD, USA

12 ³University of Maryland Baltimore County, Baltimore, MD, USA

13 ⁴University Space Research Association, Goddard Earth Sciences Technology and Research
14 (GESTAR), Columbia, MD, U.S.

15 ⁵Institute of Arctic & Alpine Research, University of Colorado, Boulder, CO, USA

16 ⁶Department of Chemistry, University of California, Irvine, Irvine, CA, USA

17 ⁷National Center for Atmospheric Research, Boulder, CO, USA

18 ⁸NASA Langley Research Center, Hampton, VA, USA

19

20 *Corresponding Author: ahsouri@cfa.harvard.edu

21

22

23

24 **Abstract.** The nonlinear chemical processes involved in ozone production ($P(O_3)$) have
25 necessitated using proxy indicators to convey information about the primary dependence of
26 $P(O_3)$ on volatile organic compounds (VOCs) or nitrogen oxides (NO_x). In particular, the ratio
27 of remotely sensed columns of formaldehyde (HCHO) to nitrogen dioxide (NO_2) has been
28 widely used for studying O_3 sensitivity. Previous studies found that the errors in retrievals and
29 the incoherent relationship between the column and the near-surface concentrations are a
30 barrier in applying the ratio in a robust way. In addition to these obstacles, we provide
31 calculational-observational evidence, using an ensemble of 0-D photochemical box models
32 constrained by DC-8 aircraft measurements on an ozone event during the Korea-United States
33 Air Quality (KORUS-AQ) campaign over Seoul, to demonstrate the chemical feedback of NO_2
34 on the formation of HCHO is a controlling factor for the transition line between NO_x -sensitive
35 and NO_x -saturated regimes. A fixed value (~ 2.7) of the ratio of the chemical loss of NO_x
36 (LNO_x) to the chemical loss of HO_2+RO_2 (LRO_x) perceptibly differentiates the regimes.
37 Following this value, data points with a ratio of HCHO/ NO_2 less than 1 can be safely classified
38 as NO_x -saturated regime, whereas points with ratios between 1 and 4 fall into one or the other
39 regime. We attribute this mainly to the HCHO- NO_2 chemical relationship causing the transition
40 line to occur at larger (smaller) HCHO/ NO_2 ratios in VOC-rich (VOC-poor) environments. We
41 then redefine the transition line to $LNO_x/LRO_x \sim 2.7$ that accounts for the HCHO- NO_2 chemical
42 relationship leading to $HCHO = 3.7 \times (NO_2 - 1.14 \times 10^{16} \text{ molec.cm}^{-2})$. Although the revised
43 formula is locally calibrated (i.e., requires for readjustment for other regions), its mathematical
44 format removes the need for having a wide range of thresholds used in HCHO/ NO_2 ratios that
45 is a result of the chemical feedback. Therefore, to be able to properly take the chemical
46 feedback into consideration, the use of $HCHO = a \times (NO_2 - b)$ formula should be preferred to
47 the ratio in future works. We then use the Geostationary Trace gas and Aerosol Sensor
48 Optimization (GeoTASO) airborne instrument to study O_3 sensitivity in Seoul. The
49 unprecedented spatial ($250 \times 250 \text{ m}^2$) and temporal (\sim every two hours) resolutions of HCHO
50 and NO_2 observations from the sensor enhance our understanding of $P(O_3)$ in Seoul; rather than
51 providing a crude label for the entire city, more in-depth variabilities in chemical regimes are
52 observed that should be able to inform mitigation strategies correspondingly.

53 **Keywords:** ozone sensitivity, remote sensing, formaldehyde, NO_2 , emissions, modeling

54 **Introduction**

55 The study of ozone concentrations in the troposphere is complicated by a number of
56 factors including the nonlinearity of the net ozone production ($P(O_3)$) to its precursor sources,
57 primarily from nitrogen oxides (NO_x) and volatile organic compound (VOC) emissions

58 [Sillman, 1999]. To precisely determine this complex chemical relationship, we either need to
59 i) measure NO_x , VOC, and their chemical reactivity or ii) set up a well-established chemical
60 transport model that can fairly reproduce the relevant species abundance. The former
61 alternative is limited to spatially-sparse observations collected from campaigns and the latter
62 is too optimistic given the underlying errors associated with model inputs and mechanisms
63 [e.g., Choi and Souri, 2015a]. In absence of these models and observations, chemical proxies
64 can be used to provide some insights into the ozone- NO_x -VOC relationship. Sillman [2002]
65 validated the robustness of several proxy indicators and found $\text{H}_2\text{O}_2/\text{HNO}_3$ to be a solid way
66 to diagnose O_3 sensitivity. This ratio is strongly proportional to the chemical loss of HO_2+RO_2
67 (LRO_x) over the chemical loss of NO_x (LNO_x) which was revisited later in Schroeder et al.
68 [2017] who found it to be a reliable metric to locate the ridgelines in $\text{P}(\text{O}_3)$ isopleths.
69 Unfortunately, the satellite-based measurements of these two compounds are limited to scarce
70 limb soundings with limited sensitivity to the boundary layer [Mencaraglia et al., 2006;
71 Rinsland et al., 2007].

72 The absorption lines of several molecules in UV-Visible spectral range allow the
73 retrieval of HCHO [e.g., Chance et al., 1991, 1997, 2000; González Abad et al., 2015; De
74 Smedt et al., 2015], and NO_2 [e.g., Martin et al., 2002; Boersma et al., 2002; Marchenko et al.,
75 2015] from space [González Abad et al., 2019]. The availability of these observations with
76 high spatial coverage has motivated scholars to leverage HCHO and NO_2 concentrations as
77 proxies for VOC reactivity and NO_x , respectively [Tonnensen, and Dennis, 2000]. Using a
78 synergy of model simulations and the Global Ozone Monitoring Experiment (GOME)
79 HCHO/ NO_2 observations, Martin et al. [2004] made an early attempt showing that surface
80 ozone production is more sensitive to NO_x than VOCs during the summers in Northern
81 Hemisphere. Duncan et al. [2010] combined models and Ozone Monitoring Instrument (OMI)
82 data to show certain ranges of HCHO/ NO_2 ratios that can be useful for classifying a region into
83 NO_x -sensitive (i.e. NO_x -limited) or NO_x -saturated (i.e. VOC-limited) regimes. Following these
84 results, the ratio has been widely used for studying weekly variations in HCHO/ NO_2 ratios over
85 the U.S. [Choi et al., 2012], its long term trends in Iran [Choi and Souri, 2015b], Texas [Choi
86 and Souri, 2015a], East Asia [Jin and Holloway, 2015; Souri et al., 2017], Colorado [Schroeder
87 et al., 2017; Jeon et al., 2018], and on a global scale [Jin et al., 2017]. A study of the relative
88 changes of the magnitude of the ratio in time and space is relevant; but the challenge is to
89 whether we can quantitatively rely on the absolute values to complementarily inform emission
90 regulations. A number of studies observed that differing HCHO/ NO_2 thresholds differentiate
91 the transition in the chemical regimes [e.g., Schroeder et al., 2017; Jin et al., 2017]. They

92 suggested that the fuzziness in the thresholds arises mainly from the uncertainties associated
93 with the retrievals, and the variable relationship between the column and the near-surface
94 concentrations. While those sources of errors unquestionably limit the applications of column
95 HCHO/NO₂, we hypothesize that inherent dependence of HCHO production on NO_x levels
96 [Wolfe et al., 2016] can systematically result in varying HCHO/NO₂ thresholds, regardless. To
97 investigate this hypothesis, we will focus on a chemically complex city in East Asia, Seoul,
98 during the Korean-United States Air Quality (KORUS-AQ) campaign period. We will simulate
99 an ensemble of 0-D box models constrained by aircraft observations, and validate the
100 hypothesis to be able to reformulate the transition line to reflect the chemical conditions more
101 realistically.

102 The advantage of focusing on the KORUS-AQ campaign period is the availability of a
103 large suite of observations including those from airborne remote sensing [Nowlan et al., 2016;
104 Nowlan et al., 2018; Souri et al., 2018], and in situ aircraft DC-8 observations. Particularly, we
105 will use NO₂ and HCHO observations from the Geostationary Trace gas and Aerosol Sensor
106 Optimization (GeoTASO) sensor. Because of relatively small footprint, several overpasses in
107 a course of a day, solid sensor calibration, and the use of a very detailed surface bidirectional
108 reflectance distribution function (BRDF), these airborne remote sensing measurements can be
109 partly regarded as a proxy for the upcoming first geostationary satellite for monitoring air
110 pollution in the U.S. by the Tropospheric Emissions: Monitoring Pollution (TEMPO)
111 instrument [Chance et al., 2019; Zoogman et al., 2017], in East Asia by Geostationary
112 Environment Monitoring Spectrometer (GEMS, Kim et al., 2019), and in Europe by the
113 Sentinel-4 mission [Ingmann et al., 2012]. Using the airborne observations will allow us to
114 understand to what extent we can classify the chemical conditions regimes by taking into
115 account the reformulated transition line.

116 **GeoTASO**

117 Hyperspectral airborne images in the ultraviolet-visible spectrophotometry range 290
118 nm to 695 nm were captured by two 2-D CCD detector arrays using the Geostationary Trace
119 gas and Aerosol Sensor Optimization (GeoTASO) instrument [Leitch et al., 2014]. The sensor
120 was mounted on-board NASA's B200 aircraft flying at ~9 km altitude above sea level. A more
121 detailed description of the engineering configuration for this sensor can be found in Nowlan et
122 al. [2016]. Similar to other remotely sensed instruments, the size of the footprint is a function
123 of sensor geometry, aperture, aircraft speed, altitude, and targeted signal-to-noise ratios. The
124 synergy of all this factors resulted in a 250×250 m² spatial resolution which is ~300 times as
125 fine as that of the TROPOspheric Monitoring Instrument (TROPOMI) nadir pixels. A major

126 improvement in the sensor design compared to its former campaigns was a mirror replacement.
127 This change led to mitigating stray light in the UV range, allowing for achieving a more robust
128 retrieval.

129 The HCHO retrieval algorithm follows a conventional 2-step procedure: i) HCHO slant
130 column is retrieved via direct non-linear least-squares fitting of a GeoTASO radiance spectrum
131 (328.5 nm- 356.5 nm) taking into consideration wavelength registration, slit function
132 calibration, under-sampling, closure polynomials that represent low frequency effects of
133 aerosols and molecular scattering, interference molecules (e.g., O₃ and NO₂), and rotational
134 Raman scattering [Chance et al., 2000; Nowlan et al., 2016; 2018], ii) HCHO vertical column
135 is obtained by applying an air mass factor (AMFs) to each observation quantifying the light
136 path through a simulated atmosphere using VLIDORT [Nowlan et al., 2016; 2018]. The first
137 step requires a reference spectrum as a function of cross-track position, which is determined
138 from spectra collected over a relatively clean region in the Taebaek Mountains on 25 May. The
139 earthshine reference is preferred to a solar one because it permits more efficient removal of
140 cross-track striping and biases [Nowlan et al., 2016; 2018]. The details of the retrieval and
141 possible source of uncertainty for this product can be found in Nowlan et al. [2016]. The
142 projected fitting uncertainty on the vertical column is found on average to be 3.53×10^{15}
143 molec.cm⁻² in our case study.

144 The NO₂ retrieval follows the similar procedure done for HCHO, but with a different
145 fitting window (425-460 nm) using the Differential Optical Absorption Spectroscopy (DOAS)
146 technique. NO₂ vertical column density (VCD) data below the aircraft using the algorithm
147 discussed in detail in Lamsal et al. [2017], with additional improvement for identification of a
148 relatively pollution free reference location for the spectral fitting process by analyzing Pandora
149 NO₂ observations at Songchon on 20 May, and proper accounting of NO₂ amount over the
150 reference location. To convert the differential slant column densities (dSCDs) from the DOAS
151 fit to VCDs, AMFs are calculated using the on-line radiative transfer calculation from
152 VLIDORT. Inputs to the AMF calculation include the solar and observation geometry, high-
153 resolution (1 km) Moderate Resolution Imaging Spectroradiometer (MODIS) BRDF [Schaaf
154 et al., 2011] to provide an intrinsic characterization of surface anisotropy, and diurnally-varying
155 NO₂ vertical profiles from a regional model constrained by OMI-derived NO_x emissions
156 [Goldberg et al., 2019]. The latter two are spatially interpolated to the GeoTASO footprint.
157 Other details on the retrievals and their uncertainties can be found in Lamsal et al. [2017]. For
158 both data we consider only cloud-free pixels using cloud flags provided in the data.

159

160 **An Ensemble of Photochemical Box Models**

161 In order to calculate the chemical reaction rates of several species, we use the
162 Framework for 0-D Atmospheric Modeling (F0AM) v3.1 [Wolfe et al., 2016]. The chemical
163 mechanism deployed for the calculation is based on CB6r2 [Hildebrandt Ruiz and Yarwood,
164 2013] which includes more than 77 species and 216 chemical reactions. We use observations
165 available on the DC8 platform for constraining the model by holding their values constant
166 throughout model step. This includes the required meteorological variables, photolysis
167 frequencies, and concentrations of various compounds. The averaging time for the observations
168 is 10 s. Table 1 lists inputs and configurations used for the model. Since the target of this study
169 focuses on the well-mixed boundary layer, we only incorporate those observations that are
170 within this layer based on the study of Sullivan et al. [2019]. Therefore, we limit our study to
171 afternoon only times, as the aircraft did not fly low enough during the morning. In about 15%
172 of cases, we observe missing values in some compounds (VOC-specified gases sampling have
173 different temporal resolutions). Accordingly, we fill the missing values using linear
174 interpolation. For each sample, we assume that rapidly cycling species are in a diel steady state
175 indicating that the loss and production of most of the reactive species are in balance. To be able
176 to fulfill our assumption, we run the box model for five solar cycles consecutively. It is worth
177 mentioning that the steady state assumption may not be valid if the air parcel is in the proximity
178 of high emitters [Thornton et al., 2002]. The model integration time for each solar cycle is set
179 to 30 min. To prevent the long-lived species from accumulating over time (due to the lack of
180 transport and deposition components in the box model), we use a dilution constant equal to a
181 24-h lifetime.

182 To account for measurement random noises, we perform the simulation in a stochastic
183 framework. Accordingly, in this study, the framework of the box modeling is based on an
184 ensemble model ($R_i : i = 1, 2, \dots, k$) with 50 members ($k=50$) generated by applying
185 randomness to the chemical compounds used for constraining the model. We focus on only
186 perturbing the gas concentrations to generate the ensemble models. The randomness
187 coefficients applied to each compound are drawn from a lognormal distribution with a mean
188 of 1, and a variance equal to the measurement precision listed in Table 1.

189 One can calculate the mean ($\bar{\mathbf{R}}$) and covariance (\mathbf{P}) of the reaction rates from an
190 ensemble of the box models:

$$\bar{\mathbf{R}} = \frac{1}{k} \sum_{i=1}^k \mathbf{R}_i \quad (1)$$

$$\mathbf{P} = \frac{1}{k-1} \sum_{i=1}^k (\mathbf{R}_i - \bar{\mathbf{R}})(\mathbf{R}_i - \bar{\mathbf{R}})^T \quad (2)$$

$$= \frac{1}{k-1} \mathbf{R}\mathbf{R}^T, \text{ where } \mathbf{R} \text{ is the vector of } \mathbf{R}_i - \bar{\mathbf{R}} \text{ (i.e., perturbations)}$$

191 Therefore, we are able to estimate a distribution for a number of variables including net ozone
 192 production (P(O₃)), LRO_x, LNO_x, and VOC reactivity (VOCR) rates. We calculate P(O₃) by
 193 subtracting ozone loss mainly controlled by HO_x (HO+HO₂), the formation of HNO₃, and O₃
 194 photolysis followed by the reaction of O(¹D) with water vapor from ozone formation (through
 195 removal of NO via HO₂ and RO₂) [Kleinman, 2005]:

$$P(O_3) = k_{HO_2+NO}[HO_2][NO] + \sum k_{RO_{2i}+NO}[RO_{2i}][NO]$$

$$- k_{OH+NO_2+M}[OH][NO_2][M] - P(RONO_2) \quad (3)$$

$$- k_{HO_2+O_3}[HO_2][O_3] - k_{OH+O_3}[OH][O_3]$$

$$- k_{O(^1D)+H_2O}[O(^1D)][H_2O] - L(O_3 + \textit{alkenes})$$

196 VOCR is calculated as the sum of the product of the rate constants of VOC+OH reactions
 197 (*k_{i,OH}*) and VOC concentration:

$$VOCR = \sum_i k_{i,OH+VOC_i}[VOC_i] \quad (4)$$

198 LRO_x is defined through the sum of primarily radical-radical reactions:

$$LRO_x = k_{HO_2+HO_2}[HO_2]^2 + \sum k_{RO_{2i}+HO_2}[RO_{2i}][HO_2]$$

$$+ \sum k_{RO_{2i}+RO_{2i}}[RO_{2i}]^2 \quad (5)$$

199 LNO_x mainly occurs via the NO₂+OH reaction:

$$LNO_x = k_{OH+NO_2+M}[OH][NO_2][M] \quad (6)$$

200 Figure 1 demonstrates important interactions involved in the formation of tropospheric
 201 ozone. Per one RO_x cycle (in the center of diagram), two molecules of ozone are generated.
 202 The availability of NO₂ and VOC concentrations dictates the controlling factor for driving the
 203 cycle. Assuming NO_x>>VOC leads to the removal of OH and NO₂ from the system (LNO_x)
 204 making P(O₃) a function of VOC (NO_x-saturated). On the other hand, an environment with a
 205 NO_x<<VOC undergoes a change by which it loses HO₂ and RO₂ (LRO_x) molecules rendering
 206 P(O₃) dependent on NO_x concentrations (NO_x-sensitive). Hence, the ratio of LNO_x to LRO_x
 207 offers a way to separate these two chemical condition regimes.

208 WRF-CMAQ

209 We simulate the atmospheric composition in East Asia using the CMAQ model [Byun
 210 and Schere, 2006] at 27 km spatial resolution with 328×323 grid size. We choose the CB05

211 gas-phase mechanism and the six-generation aerosol mechanism (AERO6). The location of
212 this domain is shown in Figure 2. We process anthropogenic emissions for the CMAQ domain
213 from the MIX emissions inventory 2010 [Li et al., 2015], which contains gridded ($0.25^\circ \times 0.25^\circ$)
214 monthly emissions for black carbon, carbon monoxide (CO), carbon dioxide (CO₂), NO_x,
215 ammonia (NH₃), organic carbon (OC), fine and coarse particulate matter (PM_{2.5} and PM₁₀),
216 sulfur dioxide (SO₂), and NMVOC in the CB05 mechanism. A diurnal factor adopted from the
217 EPA NEI2011 emissions is applied for the mobile sector. The FINN v1.6 emissions
218 [Wiedinmyer et al., 2011] are extended to include biomass burning emissions with
219 consideration of a plume height assumption commonly used in the GEOS-Chem model. For
220 biogenic emissions, we use a standalone MEGAN (v2.1) [Guenther et al., 2006] model
221 (offline), which incorporates a dynamic leaf area index from MODIS, a comprehensive
222 climatology of plant functional maps (PFT) [Ke et al., 2012], and meteorological fields from
223 the following weather model. In order to simulate the mesoscale meteorology, we use the
224 Weather Research and Forecasting model (WRF) v3.9.1 [Skamarock et al., 2008]. The
225 domain's grid is 342 steps west-east, 337 steps south-north, and 28 vertical pressure sigma
226 levels. We use the ACM2 scheme [Pleim, 2007] for the planetary layer fluxes, Kain-Fritsch for
227 cumulus parameterization [Kain, 2004], the WRF Single-Moment (WSM) 6-class scheme for
228 microphysics [Hong and Lim, 2006], Noah Land-Surface Model for the surface physics [Chen
229 and Dudhia, 2001], and Rapid Radiative Transfer Model (RRTM) for short- and long-wave
230 radiation. We account for the horizontal turbulent diffusion based on the standard Smagorinsky
231 first-order closure. The lateral boundary conditions and the grid nudging inputs come from the
232 global Final (FNL) 0.25° resolution model. The diurnally lateral chemical conditions are
233 generated by GEOS-Chem v10 [Bey et al., 2001] with the full chemistry mechanism (NO_x-O_x-
234 HC-Aer-Br) spun up for a year.

235 **Case Description**

236 Between April and June 2016, a joint team of researchers from the U.S. and South
237 Korea conducted an atmospheric chemistry field campaign over the Korean Peninsula and
238 surrounding open waters [<https://espo.nasa.gov/korus-aq>, last access: 22 June 2019)].
239 Observations were collected from a variety of observing systems encompassing surface sites,
240 airborne remote sensing, and in-situ aircraft observations. Figure 3 shows contour maps of
241 simulated surface ozone concentrations overlapped by 500 mb geopotential heights and 700
242 mb wind vectors in East Asia during the June 7th-10th 2016 period. A low pressure system aloft
243 over the very northern part of China associated with the trough (purple line) is responsible for
244 carrying on the continental polluted air masses from the west while obstructing those from

245 clean maritime regions coming from the south. In addition, the development of an
246 atmospherically stagnant condition over the North China Plain and the Yellow Sea from June
247 8th till June 9th 2016, evident in the expansion of the isobars, resulted in elevated ozone
248 concentrations over East Asia. For instance, ozone levels within the first 2 km altitude on June
249 9th 2016 around the Seoul metropolitan area are found to be 107 ± 14 ppbv [Figure S1]. By virtue
250 of the favorable atmospheric conditions for the formation of ozone, and the availability of
251 qualified GeoTASO and DC8 observations on June 9th 2016, we focused our study on this
252 ozone episode day. It is worth noting that on any other day during the campaign, the
253 coincidence of GeoTASO and DC8 measurements was suitable to draw statistically significant
254 conclusions on the relationship between $P(O_3)$ and ozone precursors.

255 **Ozone chemistry analysis during the episode — DC8**

256 Prior to assessing the usefulness of GeoTASO at pinpointing the sensitivity of ozone to
257 its precursors, we find it essential to study the relevant chemical rates at which ozone is being
258 formed/removed. We first validate the performance of the ensemble of box models by
259 comparing OH and HO₂ measurements to the simulated values, and those from NASA Langley
260 Research Center (LaRC) box model (<https://www-air.larc.nasa.gov/cgi-bin/ArcView/korusaq>,
261 Last access: Dec 2019). Comparing to the observations, we observe a reasonable performance
262 in our box model with respect to correlation and bias for OH ($R^2=0.43$, +27%) and HO₂
263 ($R^2=0.71$, -20%). Moreover, both box models agree well within 10% and 34% range in terms
264 of OH and HO₂, respectively [Figure S2 and S3]. Figure 4 shows the DC-8 measurements of
265 NO₂, HCHO, O₃ below 2 km, and the simulated VOCR from the box model on June 9th 2016
266 afternoon (1400-1600 LST). The borders are administration subdivisions. The rough threshold
267 of mixing layer height is derived from ceilometer backscatter profiles shown in Sullivan et al.
268 [2019]. The altitude of the aircraft is demonstrated in Figure S4. To gather a better qualitative
269 picture of the spatial variations in NO₂ and HCHO, we plot their vertical columns observed by
270 GeoTASO in the background. We find a fair correlation ($R^2=0.47$ for HCHO, and $R^2=0.69$ for
271 NO₂) between the collocated pixels and the DC-8 measurements within a 500 m radius.

272 Not surprisingly, high concentrations of NO₂ are seen in the city mainly due to
273 anthropogenic NO_x emissions. The MIX-Asia 2010 emissions inventory suggest that the
274 primary source of NO_x emissions in the Seoul metropolitan area is the mobile sector (67%, 74
275 ton/day) followed by the residential (22%, 21 ton/day) (not shown). The measured NO₂
276 columns pinned to the city are exceptionally high (~ 3.1 DU = 8.3×10^{16} molec.cm⁻²) such that
277 Pandora ground-based NO₂ column observations located in Yonsei University (Seoul) from
278 16th May to 11th June 2016 only observed such a value or higher with less than 1% occurrence

279 [Herman et al., 2018].

280 The retrieval of HCHO has intrinsically been difficult primarily due to the weaker
281 molecular absorption which leads to a relatively higher detection limit and noisier values
282 [Chance et al., 1991, 2000]. As a result, former studies mapping HCHO values on urban scales
283 using satellite observations had to oversample years of data at a cost of losing temporal
284 information [Zhu et al., 2014; Souri et al., 2017; Zhu et al., 2018]. The uniqueness of GeoTASO
285 lies in its capability to observe elevated HCHO values at sub-urban scales with just one
286 overpass [Nowlan et al., 2016], as seen in Figure 4. Souri et al. [2017] calculated the average
287 total HCHO columns from the Ozone Monitoring Instrument (OMI) in 2005-2014 and found
288 them to be comparatively high over Seoul, possibly a result of anthropogenic emissions.
289 Similarly, the combination of GeoTASO and DC-8 observations reveals a pronounced level of
290 HCHO in the urban area. A myriad of VOC compounds with various emissions sources can
291 contribute to the formation of HCHO [Seinfeld and Pandis, 2016]. A comprehensive source
292 apportionment study using VOC measurements in Seoul during the years of 2013-2015
293 suggested that the major contributor to VOC concentrations were from the solvent use and
294 mobile emissions [Song et al., 2019]. Likewise, the DC-8 aircraft measure high concentrations
295 of ethane, ethene, and methanol in the proximity of the city, all of which are largely utilized in
296 vehicle fuels [Figure S5-S7]. High toluene concentrations (a major product from solvent use)
297 are mostly observed in the southern part of the city (> 5 ppbv) [Figure S8]. As another major
298 source of VOC (and HCHO), we find high concentrations of isoprene (0.74 ± 0.23 ppbv) over
299 Seoul (Olympic Park) [Figure S9].

300 A major assumption in using HCHO/NO₂ ratio for gaining some insights into ozone
301 formation is that HCHO is a proxy for total VOCR [Duncan et al., 2010]. To reassess this
302 assumption, we plot the DC-8 HCHO versus the simulated VOCR values on June 9th 2016
303 afternoon (1400-1600 LST) in Figure 5. A significant coefficient of determination ($R^2=0.90$)
304 is found between DC-8 HCHO levels and the logarithm-transformed VOCR. The logarithmic
305 dependence indicates that two quantities begin to diverge at high values. For example, the
306 Pearson correlation coefficient between VOCR and HCHO changes from 0.9 for VOCR below
307 4 s^{-1} to 0.6 for VOCR above 4 s^{-1} . This drift is in agreement with Valin et al. [2016] who found
308 that HCHO levels under high VOCR ($>8 \text{ s}^{-1}$) are primarily dependent on OH concentrations
309 rather than VOCR at midday (see Eq 1 in the paper). Therefore, the assumption of HCHO being
310 a proxy for VOCR might not hold for VOC-rich environments.

311 A second assumption in using the ratio is that it might be a proxy for the magnitude of

312 LNO_x/LRO_x ratios [Duncan et al., 2010; Schroeder et al., 2017]. Figure 6 depicts the
313 relationship between the measured ratios versus the modeled LNO_x/LRO_x. Both quantities are
314 transformed logarithmically. A high degree of negative correlation between the two variables
315 ($R^2=0.96$) underscores the relevance of HCHO/NO₂ ratios to LNO_x/LRO_x values. Kleinman et
316 al., [2001] and Kleinman, [2005] found that P(O₃) is proportional to VO₃CR for those
317 LNO_x/LRO_x ratios near to 1 or higher (i.e., NO_x-saturated), while for lower values, it becomes
318 independent of VO₃CR (i.e., NO_x-sensitive). Schroeder et al. [2017] further reassessed this
319 indicator (i.e. LNO_x/LRO_x) during the Colorado DISCOVER-AQ campaign and found out the
320 LNO_x/LRO_x cut-off value should be increased to ~2.8 to correctly locate the P(O₃) turnaround
321 point mainly due to the inclusion of NO_z in their box model calculation. Assuming a NO_x/VOC
322 transition at LNO_x/LRO_x =1, the fitted curve in Figure 6 suggests that the transition occurs at
323 a HCHO/NO₂ ratio close to 2.8, while considering LNO_x/LRO_x=2.8 leads to the ratio ~1.8. We
324 will investigate the dependency of P(O₃) on HCHO/NO₂ ratios later.

325 In general, the observed ambient ozone concentrations neither correlate with HCHO
326 nor NO₂, as they are influenced by a combination of a non-linear chemistry, dry deposition,
327 background values, photochemistry, meteorology and stratosphere-troposphere exchange
328 [Cooper et al., 2012]. To elucidate the chemistry, we plot the major loss and formation
329 pathways in P(O₃) calculated from the box model in Figure 7. In the presence of both relatively
330 high VO₃CR rates and NO_x concentrations, we observe several ozone production hot spots
331 through the reactions of HO₂+NO and RO₂+NO over the downtown and the downwind area
332 (the predominant surface wind is weak northwesterly). The major pathway of chemical ozone
333 loss in the city is through the formation of HNO₃. O₃ photolysis by the reaction of O(¹D)+H₂O
334 is the second factor for the photochemical ozone loss. The mean P(O₃) is estimated at 7.66±2.52
335 ppbv hr⁻¹ with a maximum value up to 14.41 ppbv hr⁻¹. The elevated P(O₃) is majorly observed
336 over areas in which we see simultaneously high concentrations of HCHO (from isoprene) and
337 NO₂ [Sullivan et al., 2019].

338 To shed light on the dependency of P(O₃) on its major precursors (i.e., NO_x and VOCs),
339 we conduct two experiments; the first experiment follows an observationally stand-alone
340 framework involving the comparison of observed NO concentrations from DC-8 with P(O₃).
341 Such an experiment is limited to the range of observed values, thus to be able to extrapolate
342 the analysis, the second experiment makes use of the constrained box model changing the
343 concentrations of NO and VOCs. Here, we detach the model from the HCHO constraint to
344 allow it to respond to changes in the primary VOCs. To perturb the values, we use a linear
345 factor stretching from 0.1 to 15 with a 0.1 step (150 values). We apply this factor to all

346 constrained VOCs and NO_x (excluding HCHO and aromatic VOCs) to be able to create a
347 150×150 grid in NO₂-HCHO space.

348 Figure 8 (left panel) demonstrates the relationship between the logarithm-transformed
349 NO and P(O₃) colored by various VOCR rates for observations further than 50 km from Seoul
350 on the same day (mainly rural). The P(O₃) values increase monotonically for all ranges of NO
351 illustrated by a high degree of correlation between them. The increases in P(O₃) relative to NO
352 are steeper for larger VOCR rates. The right panel in Figure 8 shows the same relationship but
353 for those observations closer to the city (<50 km); we find that the P(O₃) dependence on NO
354 follows a quadratic function. The P(O₃) values increase for NO<~1 ppbv, but slow down
355 afterward. Theoretically, the location of the P(O₃) turnover point depends on VOCR mainly
356 due the fact that a high reactive VOC yields a larger amount of RO₂ to react with NO [e.g.,
357 Schroeder et al., 2017]. Under high NO concentrations (a typical urban setting), air parcels
358 with high VOCR are usually associated with ample RO₂ or HO₂ molecules which enhance the
359 conversion of NO to NO₂, whereas in a low VOCR environment the radical termination
360 becomes prominent removing NO₂ from the cycle. To some extent, we observe the same
361 tendency in Figure 8, but the number of observations (over Seoul) is not adequate to statistically
362 associate the sensitivity of P(O₃) with NO given a certain VOCR rate. A striking difference
363 between the two sets of observations is having much more variability for observations close to
364 Seoul, which in turn, results in increased uncertainty in the maxima (1.2-2.46 ppbv for NO).
365 This indicates the presence of diverse emissions sources, and more complex chemical condition
366 regimes, making necessary performing the second experiment for expanding our data.

367 We next explore the P(O₃) isopleths as a function of HCHO and NO₂ concentrations
368 based on the average of all perturbed observations located in the proximity of Seoul (<50 km)
369 on June 9th (1400-1600 LST) (Figure 9). We furthermore overplot the associated LNO_x/LRO_x
370 isopleths (purple lines). The chemical transition point is found at LNO_x/LRO_x~2.7 which is in
371 strong agreement with those values reported in Schroeder et al. [2017]. At points on the right
372 side of this line, P(O₃) mostly is a function of HCHO, thus reducing VOCs turns out to be a
373 practical way to reduce P(O₃). In contrast, moving toward the left side of the line renders P(O₃)
374 dependent on NO_x concentrations. The LNO_x/LRO_x contours also hint about the relationship
375 between HCHO-NO₂-O₃. Enhancement of NO₂ concentrations leads to an exponential increase
376 in LNO_x/LRO_x, evident in the smaller changes in the x-intercepts of the LNO_x/LRO_x lines.
377 This is essentially due to that fact that the relationship between NO_x emissions and NO₂
378 concentrations changes from a linear form to an exponential one [Souri et al., 2017] mainly
379 because of the feedback of NO_x on its own lifetime. Another distinct feature is that the slope

380 of the LNO_x/LRO_x lines becomes less steeper as NO_2 concentrations increase. Under rich VOC
381 environments, the LNO_x/LRO_x ratios seem to be more buffering with respect to NO_2 changes.
382 A possible explanation for this tendency can be due to the HCHO- NO_2 relationship [Wolfe et
383 al., 2016; Chan Miller et al., 2017].

384 Martin et al. [2004] suggested that the transition between VOC-sensitive and NO_x -
385 sensitive regimes occurs at a HCHO/ NO_2 ratio of 1. Figure 9 shows that the majority of data
386 points can safely be described as NO_x -saturated as long as HCHO/ NO_2 is lower than 1. On the
387 contrary, any data point that results in a larger value than 1 may fall into either NO_x -sensitive
388 or NO_x -saturated regime. Duncan et al. [2010] defined an ambiguous region ranging from 1-2
389 and classified NO_x -sensitive regimes if HCHO/ $NO_2 > 2$. According to Figure 9, using this
390 threshold, we would misclassify a sizable proportion of the data. We observe that the
391 discrepancy between the HCHO/ $NO_2 = 2$ line and that of $LNO_x/LRO_x = 2.7$ is larger for VOC
392 rich environments. In fact, to stay on $LNO_x/LRO_x = 2.7$, HCHO/ NO_2 can have a wide extent of
393 values ranging from 1 to 4, questioning the robustness of this indicator to ascribing the
394 chemical condition regimes. Using observations measured in DISCOVER-AQ Colorado,
395 Schroeder et al. [2017] similarly discovered that a broad range of column HCHO/ NO_2 ratios
396 between 1.1 and 3.3 can fall into the ambiguous class. They attributed this to the
397 inhomogeneous vertical distributions of HCHO and NO_2 . However, there is a feature in our
398 second experiment which carries over quantitatively to the more fundamental problem which
399 is the dependence of HCHO production on NO_x [Wolfe et al., 2016]. This initial finding
400 motivates us to further investigate this relationship by comparing NO_2 concentrations with the
401 HCHO formation.

402 Figure 10a depicts the HCHO formation isopleths for different NO_2 and VOCs
403 concentrations. At low VOC environments, the HCHO formation is dampened by increasing
404 NO_2 (due to OH suppression and formation of organic nitrates), whereas at high VOC
405 conditions, the availability of RO_2 and HO_2 results in enhancing VOC oxidation (thus larger
406 HCHO formation) with respect to NO_2 for given NO_2 levels (< 6 ppbv). Revisiting Figure 9, at
407 a point that HCHO=22 ppbv and $NO_2=8$ ppbv, the $LNO_x/LRO_x = 2.7$ line suggests that this data
408 point is in NO_x -saturated while the conventional threshold (HCHO/ $NO_2 = 2$) indicates
409 otherwise. According to Figure 10a, an increase in NO_2 at this point should naturally result in
410 reducing HCHO formation, which in turn, moves this point to the bottom and the right side of
411 the $P(O_3)$ isopleth (i.e., toward NO_x -saturated regime). This provides theoretical evidence that
412 the hypothesis on this point being NO_x -sensitive regime (by HCHO/ $NO_2 = 2$) is spurious.
413 Likewise, at a point that HCHO = 2 ppbv and $NO_2 = 2$ ppbv, the transitional line indicates that

414 this point should be labeled in the NO_x-sensitive regime, whereas the threshold suggests the
 415 NO_x-saturated. The wide range of HCHO/NO₂ ratios that the transition line falls in can be
 416 partly explainable by the impact of NO₂ on HCHO formation. Under VOC-rich environments,
 417 the feedback of NO₂ on HCHO formation increases the numerator of the HCHO/NO₂ ratios
 418 (and denominator of LNO_x/LRO_x) indicating the transition occurs at larger ratios. On other
 419 hand, under VOC-poor environment, the same chemical feedback decreases the numerator
 420 suggesting that the transition occurs at the smaller ratios. The inherit dependence of HCHO
 421 formation on NO_x concentrations have comprehensively studied in Marias et al. [2012], Valin
 422 et al. [2016], and Wolfe et al. [2016]. The major driver for this chemical feedback is by OH
 423 production/loss. To better demonstrate this, we plot the contour map of OH concentration from
 424 the same analysis done for HCHO formation in Figure 10b. The figure shows enhanced OH
 425 mainly due to RO₂+NO reaction for given NO₂ concentrations (depending on the abundance
 426 of VOCs), but reduced OH afterward primary due to NO₂+OH reaction. Therefore, the more
 427 reactive a VOC compound is, the larger NO_x can boost HCHO production, thus complicating
 428 the HCHO/NO₂ ratio. We observe the same chemical tendency by calculating the derivative of
 429 HCHO columns with respect to the NO_x emissions using the CMAQ Direct Decoupled Method
 430 (DDM) [Cohan et al., 2005] during afternoon in May-June 2016 [Figure S10].

431 With this caveat in mind, we define our case-specific transition line for mapping
 432 GeoTASO columns into the different regimes by fitting a line to the LNO_x/LRO_x=2.7 which
 433 results in the following equation:

$$HCHO = 3.7 \times (NO_2 - 2.2 \text{ ppbv}) \quad (7)$$

434 It is worth pointing out here that this is for the local relationship under a well-mixed planetary
 435 boundary condition, which may not translate easily to the ratio of the columns. In fact, the
 436 variable relationship between the columns and the near-surface concentrations can provide
 437 another source of error that has been comprehensively studied in Duncan et al. [2010], Jin et
 438 al. [2017] and Schroeder et al. [2017]. However, on this specific day, the assumption of a
 439 well-mixed boundary, evident in the strong degree of correlation between GeoTASO and
 440 DC8, allowed us to isolate the chemical feedback, an overlooked error in the use of the ratio.
 441 To convert the intercept to column, we assume uniformly mixed NO₂ concentrations (2.2
 442 ppbv) from 0 to 2 km above ground level and for higher altitudes; we follow the CMAQ-
 443 WRF profiles over Seoul. The use of the model is due to the lack of DC-8 spiral
 444 measurements over Seoul on this day. The converted formula to the columns is:

$$HCHO = 3.7 \times (NO_2 - 1.14 \times 10^{16} \text{ molec. cm}^{-2}) \quad (8)$$

445

446 Mapping Chemical Conditions over Seoul — GeoTASO

447 To proceed further with the link between the transition line derived from the second
448 experiment and GeoTASO HCHO/NO₂ columns, will first require a comparison of DC-8
449 HCHO/NO₂ ratios to those of GeoTASO on June 9th 2016 at 1400-1600 LST. Figure 11 shows
450 a point-to-point comparison of these two datasets collocated spatially. The temporal co-
451 registration of both datasets is not feasible; we have to assume that both datasets are exposed
452 to the same atmospheric condition in the 1400-1600 LST window. The comparison suggests
453 that DC-8 fairly captures ~60% of the variance in GeoTASO. However, GeoTASO
454 HCHO/NO₂ ratios tend to be higher than those of DC-8. A number of factors contribute to the
455 disagreement between two datasets: i) the accuracy in the retrievals [Nowlan et al., 2016;
456 Nowlan et al., 2018; Lamsal et al., 2017] can directly contaminate HCHO/NO₂ column, ii) the
457 assumption of the effective vertical diffusion mechanism within the mixed layer should not
458 rule out the impact of the free troposphere on the magnitude of column, and iii) the spatial
459 heterogeneity in the observations inevitably leads to some degree of disagreements.

460 We further use Eq.8 to classify the Seoul metropolitan area into NO_x-saturated and
461 NO_x-sensitive regimes at different times of the day (1000-1600 LST), shown in Figure 12.
462 Compared with former studies using satellite observations [Choi and Souri, 2015a,b; Jin and
463 Holloway, 2015; Duncan et al., 2010; Choi et al., 2012; Chang et al., 2016; Jin et al., 2017;
464 Souri et al., 2017], GeoTASO with unprecedented spatial and temporal resolutions provides
465 much more in-depth information at a fine scale. In a broad picture, NO_x-sensitive regimes are
466 primarily observed in suburbs, whereas the NO_x-saturated regimes are mostly confined to urban
467 settings. Areas that are located in NO_x-saturated regime change over time, shrinking from the
468 morning time to the afternoon which is mainly associated with photochemistry, although the
469 impact of meteorology and traffic patterns cannot be neglected. We constantly observe how
470 the Olympic Park (shown with a red circle) falls into NO_x-saturated regime suggesting that the
471 abrupt increase in isoprene in this area [Figure S9] can strongly enhance P(O₃). Based on OMI
472 observations from 2005-2015, Jin et al. [2017] labeled Seoul as the transitional regime in warm
473 seasons. Integrating all pixels from GeoTASO leads to the same conclusion (assuming
474 $1 < \text{HCHO/NO}_2 < 2$ as the transitional class), suggesting that the broad picture of the latter
475 remains correct; however, the finer resolution of GeoTASO allows the regimes to be further
476 broken out into smaller segments, showing significant spatial variations in HCHO/NO₂ ratios.
477 To better demonstrate how a finer spatial resolution can be critical for our application, we chose
478 an area in Incheon by putting together the CMAQ-derived ratios in 27×27 km² and those of
479 GeoTASO, shown in Figure 13. Unfortunately, the OMI data are unavailable on this day

480 because of technical issues in the sensor; therefore we resorted to using a model for this
481 analysis. By virtue of having a large portion (63%) of NO_x-saturated regime observed by
482 GeoTASO, the CMAQ model correctly labels this area as the same category, but according to
483 GeoTASO, the sub-pixel variabilities are large suggesting that high resolution sensors offer a
484 potential basis for designing more specific mitigation strategies.

485 **Summary**

486 Persistent increases in stagnation, continental background concentrations, and
487 photochemistry go hand-in-hand and lead to an ozone extreme event in the Seoul metropolitan
488 area on June 9th 2016, making this day an interesting target to study ozone sensitivity.
489 Specifically, DC-8 measurements observed mixing-layer NO₂ and HCHO concentrations up to
490 30 and 9 ppbv respectively over the city during the afternoon, which is an indication of an
491 exceptionally degraded air quality. To study ozone chemistry, we conduct an ensemble of
492 steady-state box models constrained by qualified observations within the mixing-layer (<2 km).
493 The ensemble of models suggests elevated volatile organic compound reactivity (VOCR) rates
494 (~ 8 s⁻¹) close to the Olympic Park in eastern Seoul mainly due to abundance of both isoprene
495 and NO_x, resulting in enhancement of net ozone production rate (P(O₃)) by 12 ppbv hr⁻¹. The
496 same observations are captured in Sullivan et al. [2019].

497 We further study the P(O₃) dependency on NO by differentiating observations in rural
498 areas (>50 km far from Seoul) and urban ones (< 50 km). In the rural areas, a strong linear
499 relationship between the two quantities is found mainly due to abundant VOCs; the relationship
500 turns into a quadratic form in the urban areas resulting from NO₂+OH reaction. The maxima
501 of this quadratic function occurs at a wide range of NO (1.2-2.46 ppbv) giving a strong
502 indication of the presence of diverse emissions. We extrapolate our analysis by perturbing the
503 primary compounds and find that the loss of NO_x (LNO_x) to the loss of HO₂+RO₂ (LRO_x)
504 which is roughly equivalent to HNO₃/H₂O₂ suggested by Sillman et al. [2002] is a robust way
505 to differentiate NO_x-sensitive (i.e. NO_x-limited) or NO_x-saturated (i.e. VOC-limited)
506 [Schroeder et al., 2017]. Following the ratio of LNO_x/LRO_x~2.7 describing the transition line,
507 the conventional thresholds of HCHO/NO₂ ratios, a proxy indicator commonly applied using
508 satellite-derived observations, are not always applicable. Our theoretically observational-
509 calculational experiment indicates that NO₂-HCHO chemical relationship plays a major role in
510 usefulness of the mathematical formulation of HCHO/NO₂. Under VOC-rich environment, the
511 acceleration of HCHO formation with respect to NO₂ suggests that the transition line occurs at
512 larger HCHO/NO₂ ratios (up to 4), whereas under VOC-poor environment, the suppression of
513 HCHO formation due to NO₂ indicates that the transition line happens at the smaller ratios.

514 Our analysis highlights the limitation of using the HCHO/NO₂ ratios at pinpointing the regimes
515 from a chemical point of view. This means that the conventional approach of formulating this
516 indicator is facing problems under both VOC-rich and VOC-poor environments, thereby a
517 fundamental reformulation might be needed. We then reformulate the indicator to be able to
518 match with $LNO_x/LRO_x \sim 2.7$ which leads to $HCHO = 3.7 \times (NO_2 - 1.14 \times 10^{16} \text{ molec.cm}^{-2})$. The
519 advantage of using this mathematical format over a ratio lies in the fact that it removes the need
520 for providing a wide range of thresholds depending on VOC environment, although the
521 numbers here have been calibrated locally. This means that the coefficients provided here in
522 the new formula might not be applicable for other regions around the globe; accordingly, we
523 encourage only the use of $HCHO = a \times (NO_2 - b)$ formula in future works for other regions in
524 which the coefficients will be adjusted with respect to field measurements.

525 Making use of newly available airborne remotely sensed data at unprecedented spatial
526 and temporal resolutions, we use the redesigned formula in an effort to classify the chemical
527 condition regimes over Seoul. Compared to a crude classification suggested in former studies
528 using coarse satellite observations [Souri et al., 2017; Jin et al., 2017], the Geostationary Trace
529 gas and Aerosol Sensor Optimization (GeoTASO) airborne instrument reveals more in-depth
530 spatial and temporal variabilities associated with the regimes. We observe a larger ring of NO_x-
531 saturated regimes at 10-12 LST compared to the afternoon possibly due to less active
532 photochemistry. The Olympic Park in which P(O₃) is high is constantly observed in NO_x-
533 saturated regime throughout the daytime. Results ensure the capability of future geostationary
534 satellites at better capturing the chemical condition regimes with much improved spatial and
535 temporal coverage.

536 **Acknowledgment**

537 We thank the funding from NASA Aura Science Team (#NNX17AH47G). We acknowledge
538 the publicly available WRF, CMAQ, GEOS-Chem and KORUS-AQ data that make this study
539 possible. The simulations were run on the Smithsonian Institution High Performance Cluster
540 (SI/HPC).

541

542

543 **References**

- 544 Bey, I., Jacob, D.J., Yantosca, R.M., Logan, J.A., Field, B.D., Fiore, A.M., Li, Q., Liu, H.Y.,
545 Mickley, L.J. and Schultz, M.G., 2001. Global modeling of tropospheric chemistry
546 with assimilated meteorology: Model description and evaluation. *Journal of*
547 *Geophysical Research: Atmospheres*, 106(D19), pp.23073-23095.
- 548 Boersma, K.F., Eskes, H.J., Veefkind, J.P., Brinksma, E.J., Van Der A, R.J., Sneep, M., Van
549 Den Oord, G.H.J., Levelt, P.F., Stammes, P., Gleason, J.F. and Bucsela, E.J., 2007.
550 Near-real time retrieval of tropospheric NO₂ from OMI. *Atmospheric Chemistry and*
551 *Physics*, 7(8), pp.2103-2118.
- 552 Byun, D. and Schere, K.L., 2006. Review of the governing equations, computational
553 algorithms, and other components of the Models-3 Community Multiscale Air Quality
554 (CMAQ) modeling system. *Applied mechanics reviews*, 59(2), pp.51-77.
- 555 Chan Miller, C., Jacob, D.J., Marais, E.A., Yu, K., Travis, K.R., Kim, P.S., Fisher, J.A., Zhu,
556 L., Wolfe, G.M., Hanisco, T.F. and Keutsch, F.N., 2017. Glyoxal yield from isoprene
557 oxidation and relation to formaldehyde: chemical mechanism, constraints from
558 SENEX aircraft observations, and interpretation of OMI satellite data. *Atmospheric*
559 *Chemistry and Physics*, 17(14), pp.8725-8738.
- 560 Chance, K., 2001. OMI algorithm theoretical basis document. volume IV: OMI trace gas
561 algorithms, <https://ozoneaq.gsfc.nasa.gov/media/docs/ATBD-OMI-04.pdf>
- 562 Chance, K., J.P. Burrows, and W. Schneider, 1991. Retrieval and molecule sensitivity studies
563 for the Global Ozone Monitoring Experiment and the Scanning Imaging Absorption
564 spectroMeter for Atmospheric CHartographY. *Proc. S.P.I.E.*, 1491, 151-165,
565 doi:10.1117/12.46657.
- 566 Chance, K., J.P. Burrows, D. Perner, and W. Schneider, 1997. Satellite measurements of
567 atmospheric ozone profiles, including tropospheric ozone, from ultraviolet/visible
568 measurements in the nadir geometry: a potential method to retrieve tropospheric
569 ozone. *J. Quant. Spectrosc. Radiat. Transfer*, 57, 467-476, doi:10.1016/S0022-
570 4073(96)00157-4.
- 571 Chance, K., P. Palmer, and R. Spurr, 2000. Satellite observations of formaldehyde over North
572 America. *Geophys. Res. Lett.*, 27(21), 3461–3464.
- 573 Chance, K., X. Liu, C. Chan Miller, G. González Abad, G. Huang, C. Nowlan, A. Souri, R.
574 Suleiman, K. Sun, H. Wang, L. Zhu, P. Zoogman, J. Al-Saadi, J.-C. Antuña-Marrero,
575 J. Carr, R. Chatfield, M. Chin, R. Cohen, D. Edwards, J. Fishman, D. Flittner, J.
576 Geddes, M. Grutter, J.R. Herman, D.J. Jacob, S. Janz J. Joiner, J. Kim, N.A. Krotkov,
577 B. Lefer, R.V. Martin, O.L. Mayol-Bracero, A. Naeger, M. Newchurch, G.G. Pfister,
578 K. Pickering, R.B. Pierce, C. Rivera Cárdenas, A. Saiz-Lopez, W. Simpson, E. Spinei,
579 R.J.D. Spurr, J.J. Szykman, O. Torres, and J. Wang, TEMPO Green Paper: Chemistry,
580 physics, and meteorology experiments with the Tropospheric Emissions: Monitoring
581 of Pollution instrument, *Proc. SPIE*, In *Sensors, Systems, and Next-Generation*
582 *Satellites XXIII* (Vol. 11151, p. 111510B). International Society for Optics and
583 Photonics.
- 584 Chang, C.Y., Faust, E., Hou, X., Lee, P., Kim, H.C., Hedquist, B.C. and Liao, K.J., 2016.
585 Investigating ambient ozone formation regimes in neighboring cities of shale plays in
586 the Northeast United States using photochemical modeling and satellite retrievals.
587 *Atmospheric environment*, 142, pp.152-170.
- 588 Chen, F. and Dudhia, J., 2001. Coupling an advanced land surface–hydrology model with the
589 Penn State–NCAR MM5 modeling system. Part I: Model implementation and
590 sensitivity. *Monthly Weather Review*, 129(4), pp.569-585.

- 591 Choi, Y. and Souri, A.H., 2015a. Chemical condition and surface ozone in large cities of
592 Texas during the last decade: Observational evidence from OMI, CAMS, and model
593 analysis. *Remote Sensing of Environment*, 168, pp.90-101.
- 594 Choi, Y. and Souri, A.H., 2015b. Seasonal behavior and long-term trends of tropospheric
595 ozone, its precursors and chemical conditions over Iran: A view from space.
596 *Atmospheric Environment*, 106, pp.232-240.
- 597 Choi, Y., Kim, H., Tong, D. and Lee, P., 2012. Summertime weekly cycles of observed and
598 modeled NO_x and O₃ concentrations as a function of satellite-derived ozone
599 production sensitivity and land use types over the Continental United States.
600 *Atmospheric Chemistry and Physics*, 12(14), pp.6291-6307.
- 601 Cohan, D.S., Hakami, A., Hu, Y. and Russell, A.G., 2005. Nonlinear response of ozone to
602 emissions: Source apportionment and sensitivity analysis. *Environmental Science &*
603 *Technology*, 39(17), pp.6739-6748.
- 604 Cooper, O.R., Parrish, D.D., Ziemke, J., Balashov, N.V., Cupeiro, M., Galbally, I.E., Gilge,
605 S., Horowitz, L., Jensen, N.R., Lamarque, J.F. and Naik, V., 2014. Global distribution
606 and trends of tropospheric ozone: An observation-based review. *Elem Sci Anth*, 2.
- 607 De Smedt, I., Stavrou, T., Hendrick, F., Danckaert, T., Vlemmix, T., Pinardi, G., Theys,
608 N., Lerot, C., Gielen, C., Vigouroux, C. and Hermans, C., 2015. Diurnal, seasonal and
609 long-term variations of global formaldehyde columns inferred from combined OMI
610 and GOME-2 observations. *Atmospheric Chemistry & Physics*, 15(8).
- 611 Duncan, B.N., Yoshida, Y., Olson, J.R., Sillman, S., Martin, R.V., Lamsal, L., Hu, Y.,
612 Pickering, K.E., Retscher, C., Allen, D.J. and Crawford, J.H., 2010. Application of
613 OMI observations to a space-based indicator of NO_x and VOC controls on surface
614 ozone formation. *Atmospheric Environment*, 44(18), pp.2213-2223.
- 615 Goldberg, D. L., Saide, P. E., Lamsal, L. N., Foy, B. d., Lu, Z., Woo, J.-H., Kim, Y., Kim, J.,
616 Gao, M., Carmichael, G., and Streets, D. G.: A top-down assessment using OMI NO₂
617 suggests an underestimate in the NO_x emissions inventory in Seoul, South Korea,
618 during KORUSAQ, *Atmos. Chem. Phys.*, 19, 1801–1818,
- 619 González Abad G., Souri, A.H., Bak, J., Chance, K., Flynn, L.E., Krotkov, N.A., Lamsal, L.,
620 Li, C., Liu, X., Miller, C.C. and Nowlan, C.R., 2019. Five decades observing Earth's
621 atmospheric trace gases using ultraviolet and visible backscatter solar radiation from
622 space. *Journal of Quantitative Spectroscopy and Radiative Transfer*.
- 623 González Abad, G., Liu, X., Chance, K., Wang, H., Kurosu, T.P. and Suleiman, R., 2015.
624 Updated Smithsonian Astrophysical Observatory Ozone Monitoring Instrument (SAO
625 OMI) formaldehyde retrieval. *Atmospheric Measurement Techniques*, 8(1), pp.19-32.
- 626 Guenther, A., Karl, T., Harley, P., Wiedinmyer, C., Palmer, P.I. and Geron, C., 2006.
627 Estimates of global terrestrial isoprene emissions using MEGAN (Model of Emissions
628 of Gases and Aerosols from Nature). *Atmospheric Chemistry and Physics*, 6(11),
629 pp.3181-3210.
- 630 Herman, J., Spinei, E., Fried, A., Kim, J., Kim, J., Kim, W., Cede, A., Abuhassan, N. and
631 Segal Rozenhaimer, M., 2018. NO₂ and HCHO measurements in Korea from 2012 to
632 2016 from Pandora spectrometer instruments compared with OMI retrievals and with
633 aircraft measurements during the KORUS-AQ campaign. *Atmospheric Measurement*
634 *Techniques*, 11(8), pp.4583-4603.
- 635 Hildebrandt Ruiz, L. and Yarwood, G., 2013. Interactions between Organic Aerosol and
636 NO_y: Influence on Oxidant Production, Final report for AQRP project 12-
637 012. Prepared for the Texas Air Quality Research Program.
- 638 Hong, S.Y. and Lim, J.O.J., 2006. The WRF single-moment 6-class microphysics scheme
639 (WSM6). *Asia-Pacific Journal of Atmospheric Sciences*, 42(2), pp.129-151.
- 640 Ingmann, P., Veihelmann, B., Langen, J., Lamarre, D., Stark, H. and Courrèges-Lacoste,

641 G.B., 2012. Requirements for the GMES Atmosphere Service and ESA's
642 implementation concept: Sentinels-4/-5 and-5p. Remote Sensing of Environment,
643 120, pp.58-69.

644 Jeon, W., Choi, Y., Souri, A.H., Roy, A., Diao, L., Pan, S., Lee, H.W. and Lee, S.H., 2018.
645 Identification of chemical fingerprints in long-range transport of burning induced
646 upper tropospheric ozone from Colorado to the North Atlantic Ocean. Science of The
647 Total Environment, 613, pp.820-828.

648 Jin, X. and Holloway, T., 2015. Spatial and temporal variability of ozone sensitivity over
649 China observed from the Ozone Monitoring Instrument. Journal of Geophysical
650 Research: Atmospheres, 120(14), pp.7229-7246.

651 Jin, X., Fiore, A.M., Murray, L.T., Valin, L.C., Lamsal, L.N., Duncan, B., Folkert Boersma,
652 K., De Smedt, I., Abad, G.G., Chance, K. and Tonnesen, G.S., 2017. Evaluating a
653 space-based indicator of surface ozone-NO_x-VOC sensitivity over midlatitude source
654 regions and application to decadal trends. Journal of Geophysical Research:
655 Atmospheres, 122(19), pp.10-439.

656 Kain, J.S., 2004. The Kain–Fritsch convective parameterization: an update. Journal of applied
657 meteorology, 43(1), pp.170-181.

658 Ke, Y., Leung, L.R., Huang, M., Coleman, A.M., Li, H. and Wigmosta, M.S., 2012.
659 Development of high resolution land surface parameters for the Community Land
660 Model. Geoscientific Model Development, 5(6), pp.1341-1362.

661 Kim, J., et al., New Era of Air Quality Monitoring from Space: Geostationary Environment
662 Monitoring Spectrometer (GEMS), Bull. Amer. Meteor. Soc.,
663 <https://doi.org/10.1175/BAMS-D-18-0013.1>.

664 Kim, S., Jeong, D., Sanchez, D., Wang, M., Seco, R., Blake, D., Meinardi, S., Barletta, B.,
665 Hughes, S., Jung, J. and Kim, D., 2018. The controlling factors of photochemical
666 ozone production in Seoul, South Korea. Aerosol and Air Quality Research, 18(9),
667 pp.2253-2261.

668 Kleinman, L.I., Daum, P.H., Lee, Y.N., Nunnermacker, L.J., Springston, S.R., Weinstein-
669 Lloyd, J. and Rudolph, J., 2002. Ozone production efficiency in an urban area. Journal
670 of Geophysical Research: Atmospheres, 107(D23), pp.ACH-23.

671 Lamsal, L.N., Janz, S.J., Krotkov, N.A., Pickering, K.E., Spurr, R.J.D., Kowalewski, M.G.,
672 Loughner, C.P., Crawford, J.H., Swartz, W.H. and Herman, J.R., 2017. High-
673 resolution NO₂ observations from the Airborne Compact Atmospheric Mapper:
674 Retrieval and validation. Journal of Geophysical Research: Atmospheres, 122(3),
675 pp.1953-1970.

676 Leitch, J.W., T. Delker, W. Good, L. Ruppert, F. Murcay, K. Chance, X. Liu, C. Nowlan, S.
677 J. Janz, N. A. Krotkov, K. E. Pickering, M. Kowalewski, J. Wang, 2014, The
678 GeoTASO airborne spectrometer project, Proc. SPIE 9218, Earth Observing Systems
679 XIX, 92181H, doi: 10.1117/12.206376.

680 Li, M., Zhang, Q., Kurokawa, J.I., Woo, J.H., He, K.B., Lu, Z., Ohara, T., Song, Y., Streets,
681 D.G., Carmichael, G.R. and Cheng, Y.F., 2015. MIX: a mosaic Asian anthropogenic
682 emission inventory for the MICS-Asia and the HTAP projects. Atmos. Chem. Phys.
683 Discuss, 15(23), pp.34813-34869.

684 Mao, J., Ren, X., Chen, S., Brune, W.H., Chen, Z., Martinez, M., Harder, H., Lefer, B.,
685 Rappenglueck, B., Flynn, J. and Leuchner, M., 2010. Atmospheric oxidation capacity
686 in the summer of Houston 2006: Comparison with summer measurements in other
687 metropolitan studies. Atmospheric Environment, 44(33), pp.4107-4115.

688 Marais, E.A., Jacob, D.J., Kurosu, T.P., Chance, K., Murphy, J.G., Reeves, C., Mills, G.,
689 Casadio, S., Millet, D.B., Barkley, M.P. and Paulot, F., 2012. Isoprene emissions in
690 Africa inferred from OMI observations of formaldehyde columns. Atmospheric

691 Chemistry and Physics, 12(14), pp.6219-6235.

692 Marchenko S., N.A. Krotkov, L.N. Lamsal, E.A. Celarier, W.H. Swartz, E.J. Bucsela,
693 Revising the slant- column density retrieval of nitrogen dioxide observed by the
694 Ozone Monitoring Instrument, *J. Geophys. Res.*, DOI: 10.1002/2014JD022913, 2015.

695 Martin, R.V., Fiore, A.M. and Van Donkelaar, A., 2004. Space-based diagnosis of surface
696 ozone sensitivity to anthropogenic emissions. *Geophysical Research Letters*, 31(6).

697 Mencaraglia, F., Bianchini, G., Boscaleri, A., Carli, B., Ceccherini, S., Raspollini, P., Perrin,
698 A. and Flaud, J.M., 2006. Validation of MIPAS satellite measurements of HNO₃
699 using comparison of rotational and vibrational spectroscopy. *Journal of Geophysical*
700 *Research: Atmospheres*, 111(D19).

701 Nowlan, C.R., Liu, X., Janz, S.J., Kowalewski, M.G., Chance, K., Follette-Cook, M.B.,
702 Fried, A., González Abad, G., Herman, J.R., Judd, L.M. and Kwon, H.A., 2018.
703 Nitrogen dioxide and formaldehyde measurements from the GEOstationary Coastal
704 and Air Pollution Events (GEO-CAPE) Airborne Simulator over Houston, Texas.
705 *Atmospheric Measurement Techniques*, 11(11), pp.5941-5964.

706 Nowlan, C.R., Liu, X., Leitch, J.W., Chance, K., González Abad, G., Liu, C., Zoogman, P.,
707 Cole, J., Delker, T., Good, W. and Murcray, F., 2016. Nitrogen dioxide observations
708 from the Geostationary Trace gas and Aerosol Sensor Optimization (GeoTASO)
709 airborne instrument: Retrieval algorithm and measurements during DISCOVER-AQ
710 Texas 2013. *Atmospheric Measurement Techniques*, 9(6), pp.2647-2668.

711 Pleim, J.E., 2007. A combined local and nonlocal closure model for the atmospheric
712 boundary layer. Part I: Model description and testing. *Journal of Applied Meteorology*
713 *and Climatology*, 46(9), pp.1383-1395.

714 Pusede, S.E., Steiner, A.L. and Cohen, R.C., 2015. Temperature and recent trends in the
715 chemistry of continental surface ozone. *Chemical reviews*, 115(10), pp.3898-3918.

716 Rinsland, C.P., Coheur, P.F., Herbin, H., Clerbaux, C., Boone, C., Bernath, P. and Chiou,
717 L.S., 2007. Detection of elevated tropospheric hydrogen peroxide (H₂O₂) mixing
718 ratios in atmospheric chemistry experiment (ACE) subtropical infrared solar
719 occultation spectra. *Journal of Quantitative Spectroscopy and Radiative Transfer*,
720 107(2), pp.340-348.

721 Schaaf, C. B., Z. Wang and A. H. Strahler, Commentary on Wang and Zender-MODIS snow
722 albedo bias at high solar zenith angles relative to theory and to in situ observations in
723 Greenland, *Rem. Sen. Env.*, 115, 1296-1300, 2011.

724 Schroeder, J.R., Crawford, J.H., Fried, A., Walega, J., Weinheimer, A., Wisthaler, A., Müller,
725 M., Mikoviny, T., Chen, G., Shook, M. and Blake, D.R., 2017. New insights into the
726 column CH₂O/NO₂ ratio as an indicator of near-surface ozone sensitivity. *Journal of*
727 *Geophysical Research: Atmospheres*, 122(16), pp.8885-8907.

728 Seinfeld, J.H. and Pandis, S.N., 2016. *Atmospheric chemistry and physics: from air pollution*
729 *to climate change*. John Wiley & Sons.

730 Sillman, S. and He, D., 2002. Some theoretical results concerning O₃-NO_x-VOC chemistry
731 and NO_x-VOC indicators. *Journal of Geophysical Research: Atmospheres*, 107(D22),
732 pp.ACH-26.

733 Sillman, S., 1999. The relation between ozone, NO_x and hydrocarbons in urban and polluted
734 rural environments. *Atmospheric Environment*, 33(12), pp.1821-1845.

735 Skamarock, W.C., Klemp, J.B., Dudhia, J., Gill, D.O., Barker, D.M., Wang, W. and Powers,
736 J.G., 2005. A description of the advanced research WRF version 2 (No. NCAR/TN-
737 468+ STR). National Center For Atmospheric Research Boulder Co Mesoscale and
738 Microscale Meteorology Div.

739 Song, S.K., Shon, Z.H., Kang, Y.H., Kim, K.H., Han, S.B., Kang, M., Bang, J.H. and Oh, I.,
740 2019. Source apportionment of VOCs and their impact on air quality and health in the

741 megacity of Seoul. Environmental pollution, 247, pp.763-774.

742 Souri, A.H., Choi, Y., Jeon, W., Woo, J.H., Zhang, Q. and Kurokawa, J.I., 2017a. Remote
743 sensing evidence of decadal changes in major tropospheric ozone precursors over East
744 Asia. *Journal of Geophysical Research: Atmospheres*, 122(4), pp.2474-2492.

745 Souri, A.H., Choi, Y., Pan, S., Curci, G., Nowlan, C.R., Janz, S.J., Kowalewski, M.G., Liu,
746 J., Herman, J.R. and Weinheimer, A.J., 2018. First Top-Down Estimates of
747 Anthropogenic NO_x Emissions Using High-Resolution Airborne Remote Sensing
748 Observations. *Journal of Geophysical Research: Atmospheres*, 123(6), pp.3269-3284.

749 Sullivan, J.T., McGee, T.J., Stauffer, R.M., Thompson, A.M., Weinheimer, A., Knute, C.,
750 Janz, S., Wisthaler, A., Long, R., Szykman, J. and Park, J., 2019. Taehwa Research
751 Forest: a receptor site for severe domestic pollution events in Korea during 2016.
752 *Atmospheric Chemistry and Physics*, 19(7), pp.5051-5067.

753 Thornton, J.A., Wooldridge, P.J., Cohen, R.C., Martinez, M., Harder, H., Brune, W.H.,
754 Williams, E.J., Roberts, J.M., Fehsenfeld, F.C., Hall, S.R. and Shetter, R.E., 2002.
755 Ozone production rates as a function of NO_x abundances and HO_x production rates in
756 the Nashville urban plume. *Journal of Geophysical Research: Atmospheres*,
757 107(D12), pp.ACH-7.

758 Tonnesen, G.S. and Dennis, R.L., 2000. Analysis of radical propagation efficiency to assess
759 ozone sensitivity to hydrocarbons and NO_x: 1. Local indicators of instantaneous odd
760 oxygen production sensitivity. *Journal of Geophysical Research: Atmospheres*,
761 105(D7), pp.9213-9225.

762 Valin, L.C., Fiore, A.M., Chance, K. and González Abad, G., 2016. The role of OH
763 production in interpreting the variability of CH₂O columns in the southeast
764 US. *Journal of Geophysical Research: Atmospheres*, 121(1), pp.478-493.

765 Wiedinmyer, C., Akagi, S.K., Yokelson, R.J., Emmons, L.K., Al-Saadi, J.A., Orlando, J.J.
766 and Soja, A.J., 2011. The Fire INventory from NCAR (FINN): A high resolution
767 global model to estimate the emissions from open burning. *Geoscientific Model
768 Development*, 4(3), p.625.

769 Wolfe, G.M., Kaiser, J., Hanisco, T.F., Keutsch, F.N., de Gouw, J.A., Gilman, J.B., Graus,
770 M., Hatch, C.D., Holloway, J., Horowitz, L.W. and Lee, B.H., 2016. Formaldehyde
771 production from isoprene oxidation across NO_x regimes. *Atmospheric Chemistry &
772 Physics*, 16, pp. 2597–2610 .

773 Wolfe, G.M., Marvin, M.R., Roberts, S.J., Travis, K.R. and Liao, J., 2016. The framework
774 for 0-D atmospheric modeling (F0AM) v3. 1. *Geoscientific Model
775 Development*, 9(9), pp.3309-3319.

776 Zhu, L., Jacob, D.J., Keutsch, F.N., Mickley, L.J., Scheffe, R., Strum, M., González Abad,
777 G., Chance, K., Yang, K., Rappenglück, B. and Millet, D.B., 2017. Formaldehyde
778 (HCHO) as a hazardous air pollutant: Mapping surface air concentrations from
779 satellite and inferring cancer risks in the United States. *Environmental science &
780 technology*, 51(10), pp.5650-5657.

781 Zhu, L., Jacob, D.J., Mickley, L.J., Marais, E.A., Cohan, D.S., Yoshida, Y., Duncan, B.N.,
782 Abad, G.G. and Chance, K.V., 2014. Anthropogenic emissions of highly reactive
783 volatile organic compounds in eastern Texas inferred from oversampling of satellite
784 (OMI) measurements of HCHO columns. *Environmental Research Letters*, 9(11),
785 p.114004.

786 Zoogman, P., Liu, X., Suleiman, R.M., Pennington, W.F., Flittner, D.E., Al-Saadi, J.A.,
787 Hilton, B.B., Nicks, D.K., Newchurch, M.J., Carr, J.L. and Janz, S.J. et al., 2017.
788 Tropospheric emissions: Monitoring of pollution (TEMPO). *J. Quant. Spectro. &
789 Radiat. Transfer*, 186, 17-39, doi:org/10.1016/j.jqsrt.2016.05.008.

790

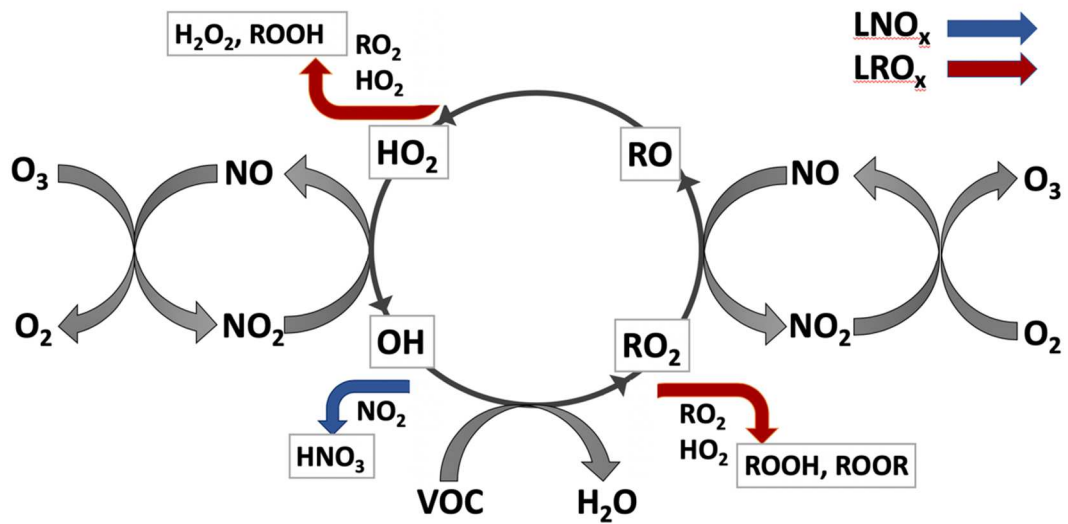
791
 792
 793 Tables
 794

Table1. The box model configurations and inputs.

Time Steps	30 mins
Number of Solar cycles	5
Dilution constant	1/86400 (s ⁻¹)
Meteorological Inputs	Pressure, Temperature, Relative Humidity
Photolysis frequencies	Measured by NCAR's CCD Actinic Flux Spectroradiometers
Chemical Levels (Instrument#*, Precision) used for constraining the box model	H ₂ (1,5%), O ₃ (2,10%), CO (4,2%), H ₂ O ₂ (5,30%), HNO ₃ (5,30%), NO ₂ (2,30%), SO ₂ (6,30%) , CH ₄ (4,0.1%), PAN (6,20%), Alkyl nitrates (10,10%), Isoprene (1,5%), Monoterpene (9,33%), HCHO (7,3.3%), Acetone (9,3%), Ethene (1,5%), Ethyne (1,5%), Ethane (1,5%), Methanol (9,3%), CHOCHO (8,15%), Propane (1,5%), Benzene (1,5%), Xylene (1,5%), Toluene (1,5%), Acetaldehyde (9,8%)
Chemical Levels (Instrument#*, Precision) used only for initializing the box model	OH (3,32%), HO ₂ (3,32%), NO (2,20%)
Chemical Mechanism	CB6r2

795
 796 * (1) UC Irvine's Whole Air Sampler (WAS), (2) NCAR 4-Channel Chemiluminescence, (3)
 797 Penn State's Airborne Tropospheric Hydrogen Oxides Sensor (ATHOS), (4) NASA Langley's
 798 Diode laser spectrometer, (5) Caltech's single mass analyzer, (6) Georgia Tech's ionization
 799 mass spectrometer, (7) The University of Colorado at Boulder's the Compact Atmospheric
 800 Multi-species Spectrometer (CAMS), (8) Korean Airborne Cavity Enhances Spectrometer, (9)
 801 University of Oslo's PTR-TOF-MS instrument, and (10) University of California, Berkeley's
 802 TD-LIF.
 803
 804

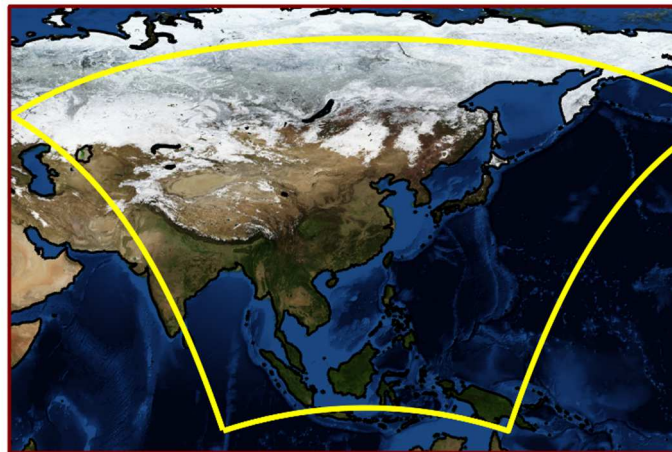
805 **Figures:**



806

807 **Figure 1.** A representation of the important interactions in the daytime chemistry of the
808 tropospheric ozone formation.

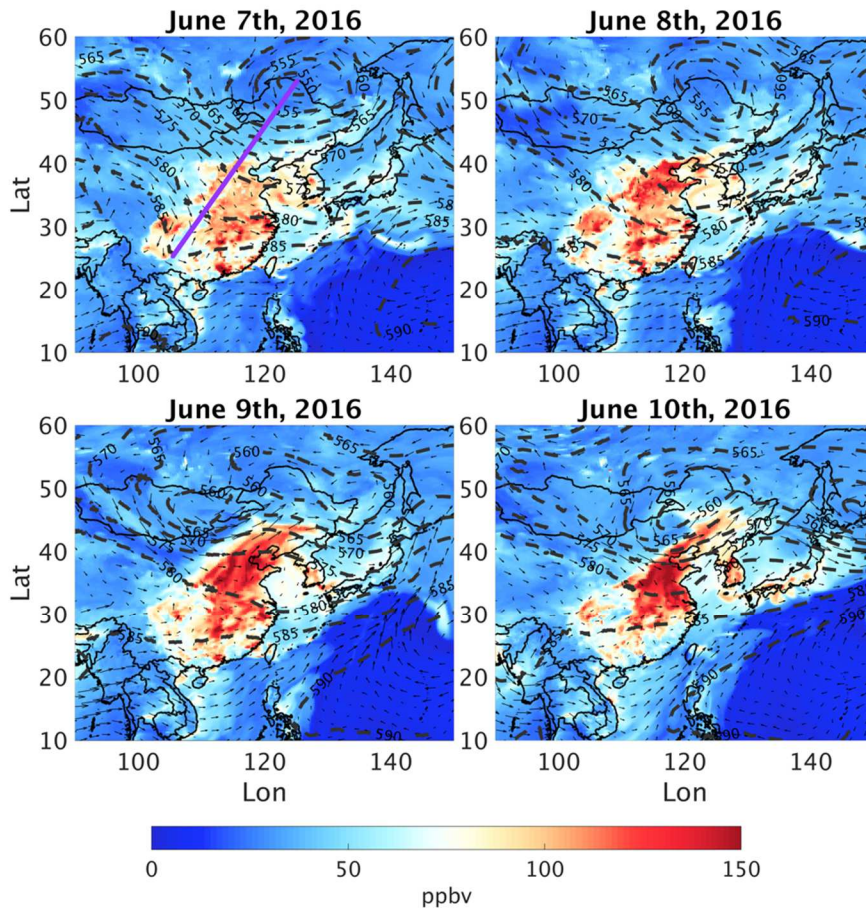
809



810

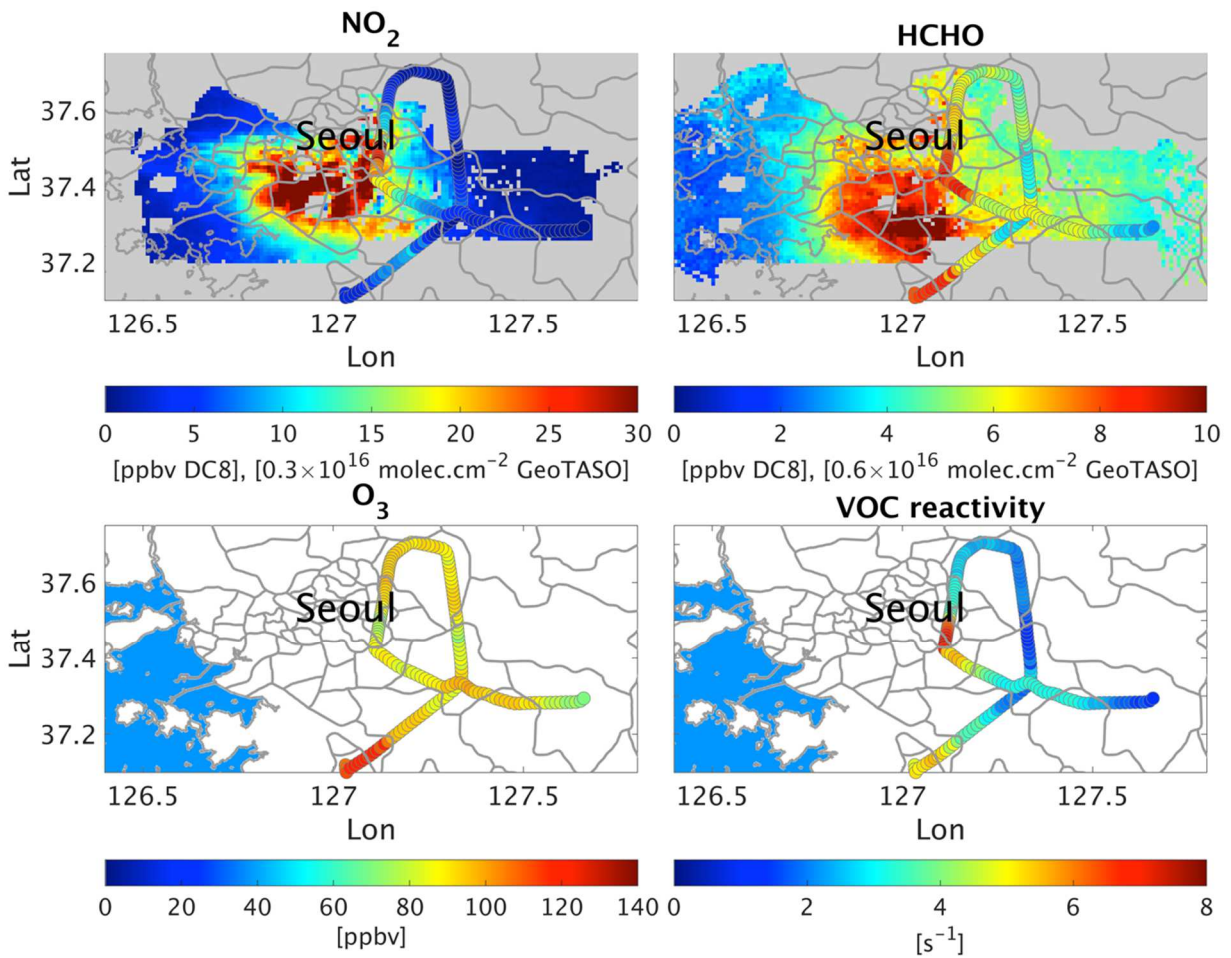
811 **Figure 2.** The location of CMAQ 27 km domain which covers China, Japan, India, South
812 Korea, Taiwan and some portions of Russia and South Asia.

813



814

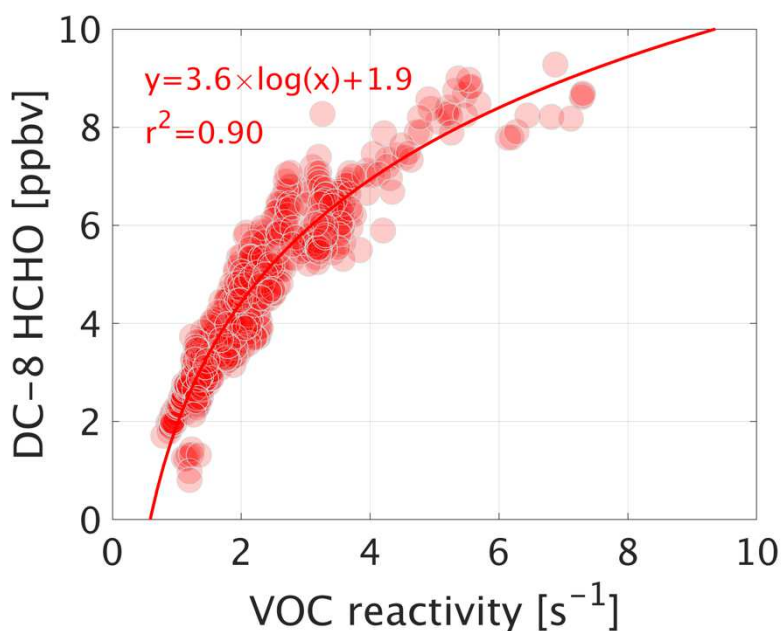
815 **Figure 3.** Synoptic-scale atmospheric conditions for East Asia at 0600 UTC on four different
 816 days (June 7th-10th 2016). The background color indicates surface ozone mixing ratios (ppbv)
 817 simulated by the WRF-CMAQ model. Black dashed lines represent 500 hPa geopotential
 818 heights (decameters), and the black vectors show 700 hPa winds.



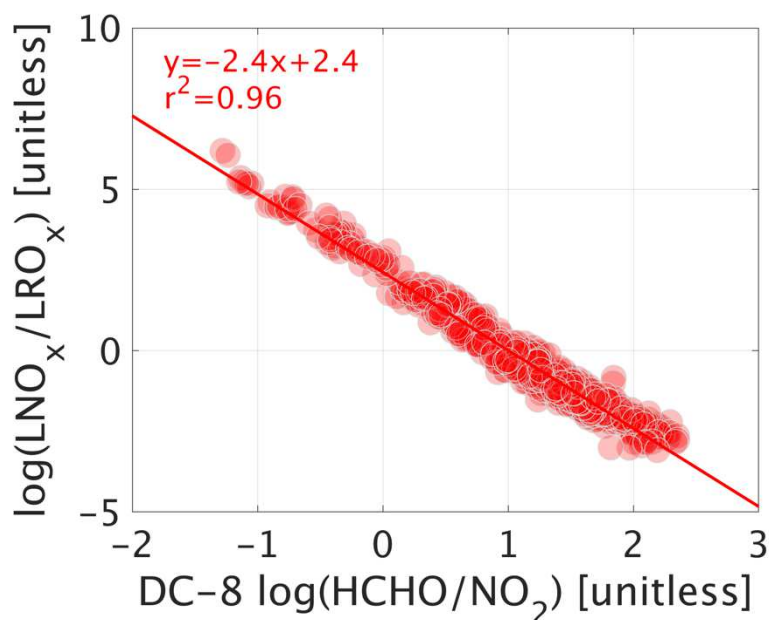
819

820 **Figure 4.** Contour maps of GeoTASO NO₂ and HCHO columns overlapped with DC-8
 821 measurements on June 9th 2016 afternoon (1400-1600 LST) (first row). The measured O₃ levels
 822 and simulated VOCR based on the ensemble of box models (second row). For inferring the
 823 columns, a factor provided in captions should be applied to the colorbar values.

824

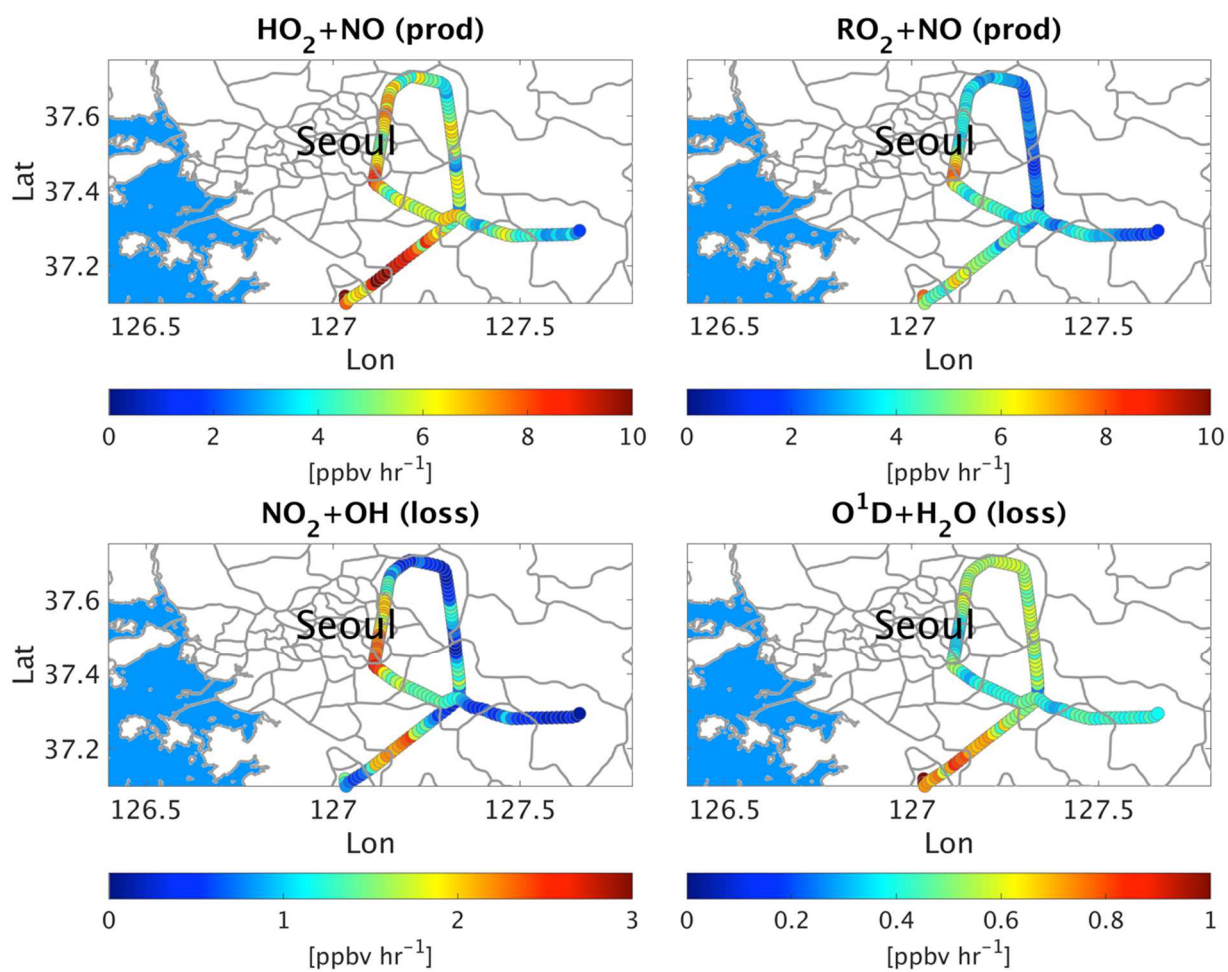


825
 826 **Figure 5.** Point-to-point comparison of simulated VOCR rates using the constrained ensemble
 827 of box models with measured HCHO values on June 9th 2016 afternoon (1400-1600 LST). Only
 828 observations with less than a 2 km altitude are considered in the analysis. The black line denotes
 829 the identity line.
 830



831
 832 **Figure 6.** Point-to-point comparison of the logarithm-transformed DC-8 HCHO/NO₂ ratios vs
 833 simulated LNO_x/LRO_x values using the constrained ensemble of box models on June 9th 2016
 834 afternoon (1400-1600 LST). Only observations with less than a 2 km altitude (mixing layer) are
 835 considered in the analysis.

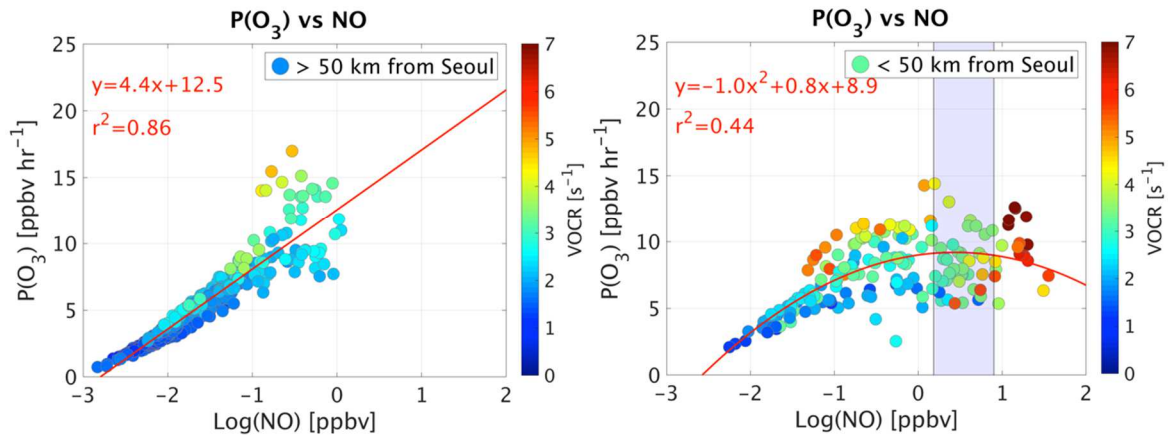
836



837

838 **Figure 7.** The simulated major pathways of photochemical ozone production (first row) and
839 loss (second row).

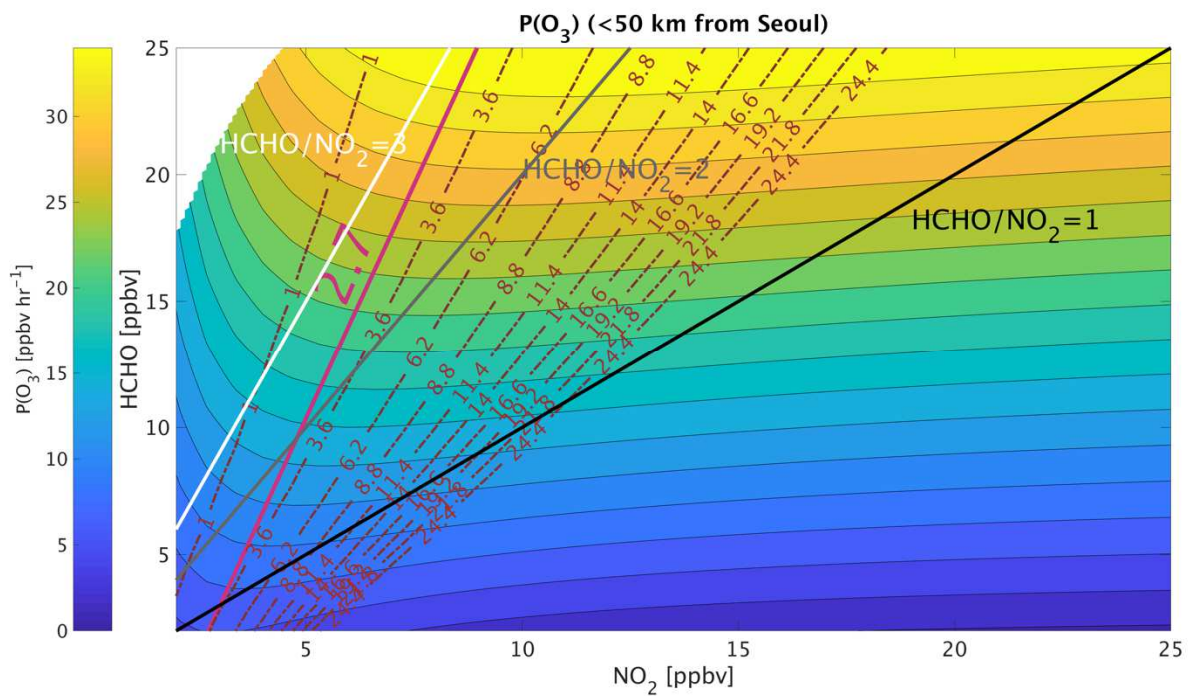
840



841

842 **Figure 8.** The relationship between observed NO and simulated P(O₃) using the constrained
 843 ensemble of box models for different regions (>50 km from Seoul in the left panel and <50 km
 844 in the right). The shade area in the right panel indicates the range of location that local maxima
 845 may fall in (at 95% confidence level).

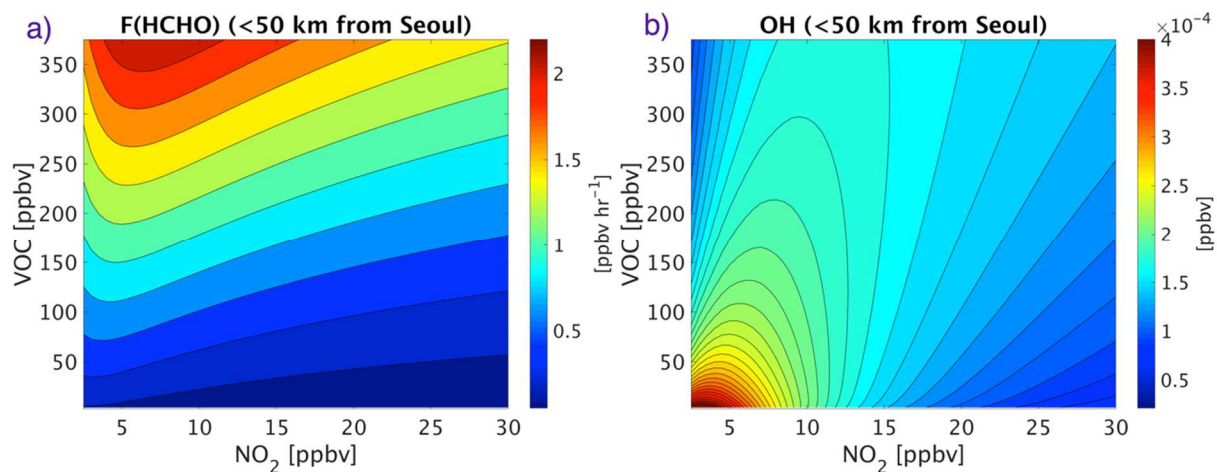
846



847

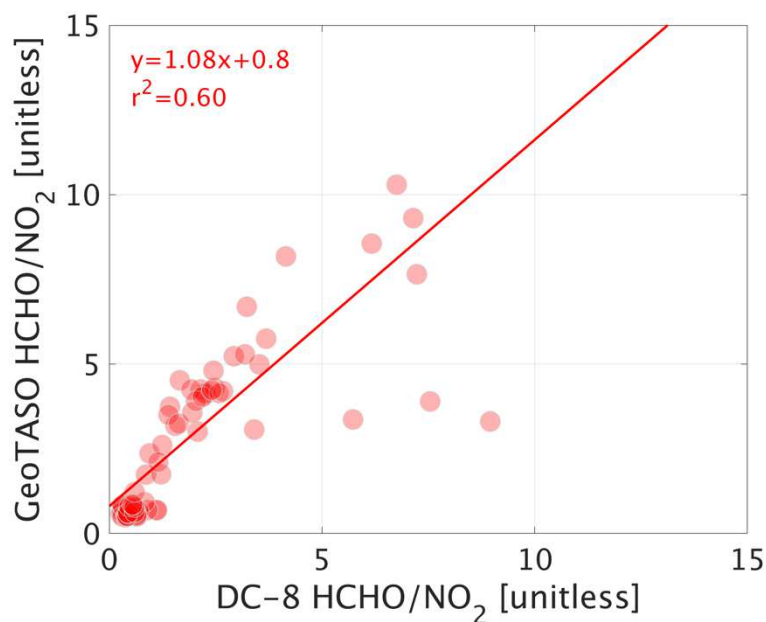
848 **Figure 9.** The P(O₃) isopleths as a function of NO₂ and HCHO concentrations overlaid by the
 849 LNO_x/LRO_x contours (purple lines). Data points used for this plot are generated by perturbing
 850 NO_x and primary VOCs (excluding HCHO and aromatic VOCs) using the box model described
 851 in Table 1. The data are collected from DC-8 on June 9th 2016 afternoon (1400-1600 LST).

852



853

854 **Figure 10.** (a) The HCHO production isopleths, and (b) the OH concentrations isopleths as a
 855 function of NO₂ and VOC concentrations.



856

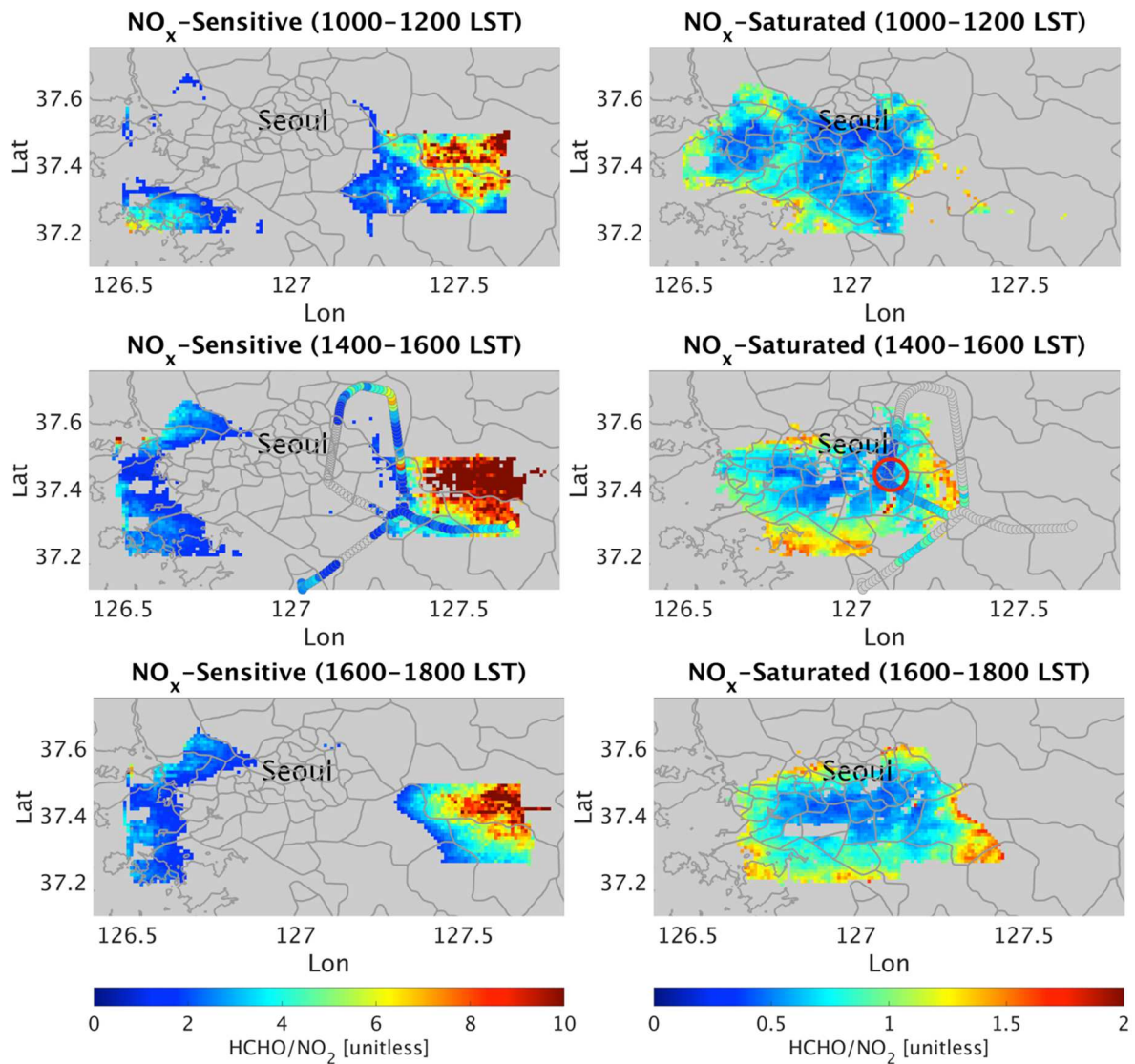
857 **Figure 11.** The comparison of GeoTASO HCHO/NO₂ ratios versus those of DC-8.

858

859

860

861



862

863

864

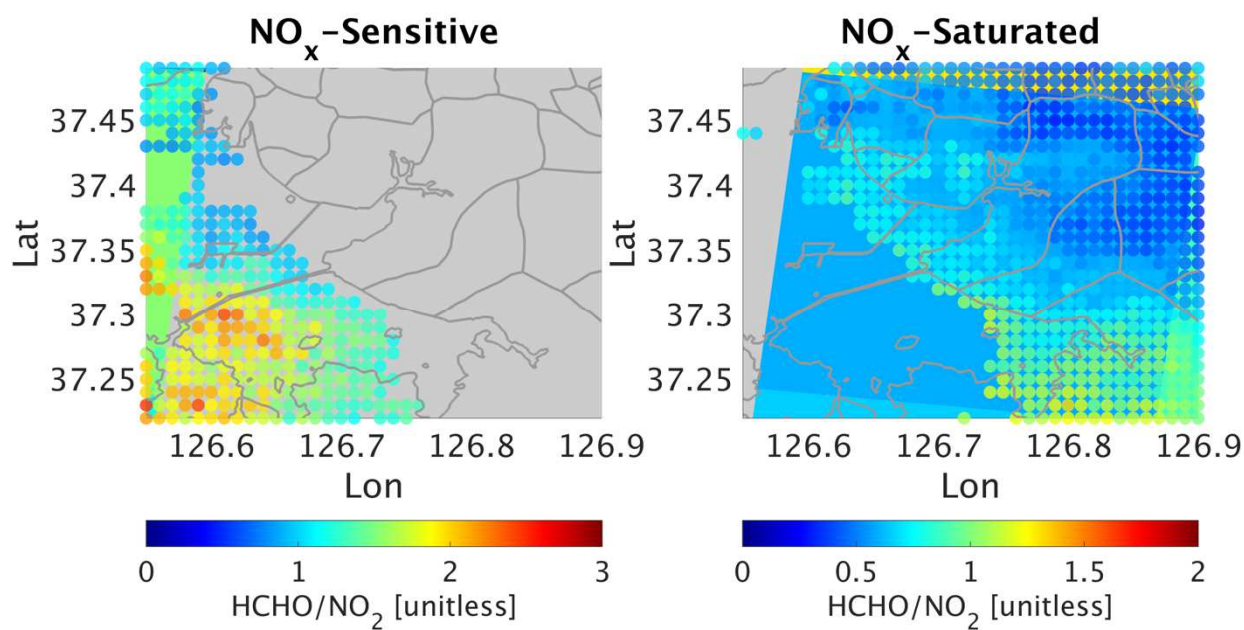
865

866

867

868

Figure 12. The contour maps of GeotASO HCHO/NO₂ ratios labeled into two different chemical conditions regimes based on the transition line derived from this study. The observations are collected on June 9th 2016. The red circle shows the location of Olympic Park.



869

870 **Figure 13.** The spatial representation of HCHO/NO₂ ratios of CMAQ (background) overlaid
 871 by those of GeoTASO for an area in Incheon, South Korea.

872